Chapter 5

Spitzer-IRS spectroscopy of the Antennae galaxies NGC 4038/39

Abstract

We observed the Antennae galaxies with the Infrared Spectrograph onboard of the Spitzer Space Telescope to study the properties of the warm interstellar medium and the most luminous super star clusters (SSCs) in this prototype merger system. We obtained high signal-to-noise $5 - 38\mu$m spectra of six super star clusters and the two galactic nuclei, as well as spectral maps of the entire central region.

By far the strongest radiation field originates from two compact clusters in the overlap region. The total star formation rate in the luminous clusters was found to be about $6 M_\odot/\mathrm{yr}$. The mid-infrared spectra of the nuclei NGC 4038 and NGC 4039 can be explained with pure star formation activity.

Regions with stronger radiation fields show reduced emission from polycyclic aromatic hydrocarbons (PAHs), but we found no evidence for ionization effects or grain size variations in the PAH spectrum. The PAH fluxes scale with the temperature of the H_2 gas suggesting that warmer photo-dissociation regions (PDRs) are more efficient PAH emitters. However, overall there is lack of spatial correspondence between H_2 and PAH emission. The temperature of the H_2 gas anti-correlates with the hardness of the radiation field, which is possibly due to a geometrical evolution of the ISM surrounding the clusters.

The average temperature of the H_2 is 295 K, and the total mass of warm H_2 is $2.5 \cdot 10^7 M_\odot$, which leads to a fraction of warm to total H_2 mass of less than **1%!!!**. We cannot confirm the exceptionally strong and extended H_2 S(3) emission that was previously reported by other authors, and rule out pre-starburst shocks resulting from galaxy interaction as the dominating excitation mechanism.

B. R. Brandl, L. Snijders, M. den Brok, D. G. Whelan, B. Groves,
V. Charmandaris, J. D. Smith, L. Armus, P. P. van der Werf & J. R. Houck

5.1 Introduction

Starbursts (e.g., Larson & Tinsley 1978; Weedman et al. 1981) play a crucial role in the cosmic star formation history, the evolution of galaxies, and the overall energy deposition in the Universe. Such starbursts often, though not exclusively, occur in interacting and colliding systems. Since collisions and interactions are believed to be a fundamental part of the evolution of galaxies in the hierarchical growth paradigm, the full characterisation of interacting galaxies is of the greatest importance in understanding the physical mechanisms that lead to a luminous starburst phase.

The Antennae galaxies, NGC 4038/39 (Arp 244), are arguably the best-known example of interacting galaxies. They are the first system in the Toomre (1977) merger sequence. In the Antennae we observe the symmetric encounter between two normal Sc type spirals at an early merger stage (Mihos & Hernquist 1996). The distance to the systems is still under debate. Earlier estimates by Stanford et al. (1990) and Wilson et al. (2000) found 20 – 21 Mpc, and Whitmore et al. (1999) determined 19.2 Mpc. Using WFPC2 to study the stellar populations at the tip of the southern tail, Saviane et al. (2004) observed the tip of the red giant branch and determined a distance of only 13.8 ± 1.7 Mpc. Unless otherwise noted we assume the distance of 21 Mpc throughout this Chapter. The Antennae's infrared luminosity between 1 – 1000 μmwas measured by the Infrared Space Observatory (ISO) to be $L_{IR} = 6.4 \cdot 10^{10} \mathrm{L}_{\odot}$(Klaas et al. 1997), just below the threshold of $10^{11} \mathrm{L}_{\odot}$necessary to qualify as luminous infrared galaxy.

The two galactic nuclei of NGC 4038 and NGC 4039, and the dust-obscured overlap region in between, exhibit one of the most stunning examples of starburst activity in the nearby Universe. The Antennae is also a showcase of why observations across the entire electromagnetic spectrum, from X-ray to the radio, are necessary to obtain a complete picture. In the following paragraphs we give a brief, and, by necessity incomplete, overview of the observations across the electromagnetic spectrum.

The first deep optical analysis of the Antennae with the Wide Field Camera on HST revealed over 700 point-like objects (Whitmore & Schweizer 1995). Subsequent observations with WFPC2 increased the sensitivity by three magnitudes in V band and revealed between 800 and 8000 clusters in four age ranges (Whitmore et al. 1999). These and related observations (e.g., Fritze-v. Alvensleben 1999) started extensive studies of extragalactic star clusters in a statistical way. Kassin et al. (2003) combined UBVRJHK images to derive extinction maps for the Antennae and found several red clusters. Brandl et al. (2005) studied the near-infrared properties of 172 clusters. Of these, a subset of 27 young (≤ 10 Myr) clusters was also detected by HST and the VLA, but no correlation was found between the infrared colors and 6 cm radio fluxes. Whitmore & Zhang (2002) also correlated optically detected star clusters with their radio counterparts from Neff & Ulvestad (2000). Mengel et al. (2005) and Fall et al. (2005) provide detailed studies of the ages and distribution of hundreds of clusters from various optical and infrared diagnostics. Gilbert et al. (2000), Gilbert & Graham (2007), and Mengel et al. (2001, 2002) investigated the properties of a few individual SSCs with near-infrared spectroscopy, and derived dynamical masses.

The Antennae provide an excellent environment to study the transformation of giant molecular clouds (GMCs) into SSCs (de La Fuente Marcos & de La Fuente Mar-

cos 2006). In a multi-wavelength study of the relationship between young star clusters and their interstellar environment, Zhang, Fall & Whitmore (2001) found evidence that both cloud-cloud collisions and shocks from recent star formation can trigger star cluster formation, but could not identify a dominant triggering mechanism. On the other hand, Whitmore et al. (2005) derived a velocity dispersion between clusters of $< 10\,\mathrm{km\,s^{-1}}$ from STIS spectroscopy and concluded that high-velocity cloud-cloud collisions cannot be the dominating starburst mode in the Antennae. Once the clusters evolve, dynamical processes may lead to their dissolution, and the observed cluster mass function will deviate from the initial cluster mass function. Fall et al. (2005) and Mengel et al. (2005) interpreted the median star cluster age of 10 Myr as evidence for rapid disruption, indicating that most of the young clusters are not gravitationally bound. In earlier studies Whitmore et al. (1999) found that the cluster luminosity function can be described by a power law, and is therefore fundamentally different from the Gaussian distribution of globular cluster masses. However, Anders et al. (2007) reported recently that a Gaussian distribution fits the observed cluster luminosity functions better than a power law. No evidence for a "non-statistical" truncation of the Antennae cluster mass function at the high mass end was found (Whitmore et al. 2007).

The first high signal-to-noise mid-infrared images of the Antennae were made by the Infrared Space Observatory. ISOCAM observations at angular resolutions of $5 - 8''$ showed that the overlap region contributes more than half of the total luminosity observed in the $12.5 - 18\mu$m range (Vigroux et al. 1996). A comparison between the HST and ISOCAM images revealed a compact, optically-obscured knot which produces 15% of the total infrared luminosity at 15 μm (Mirabel et al. 1998). From ISO-SWS spectroscopy Kunze et al. (1996) characterized the conditions of the ISM in the overlap region, and found a temperature of the warm molecular hydrogen of 405 K. Fischer et al. (1996) presented ISO-LWS observations in several far-infrared fine-structure lines and derived numerous properties of the PDR. They derive a PDR temperature of 200 K. It has been argued that collisions of gas-rich spirals produce strong shocks. Haas et al. (2005) found exceptionally strong H_2 S(3) emission in ISOCAM-CVF data, and a spatial displacement between the H_2 emission peak from the known starburst regions. They interpret these findings as evidence for pre-starburst shocks. Spitzer-IRAC $3 - 8\mu$m observations at slightly higher spatial resolution Wang et al. (2004) confirmed the ISO results and showed that the star formation rate (SFR) per unit mass in the active areas is comparable to those in starburst and some ultra-luminous galaxies. Recent subarcsecond imaging and N-band spectroscopy with VLT-VISIR resolved the H II region / PDR interface of the most luminous SSCs and revealed a highly obscured SSC that does not have an optical or near-infrared counterpart (Chapter 3, Snijders et al. 2006).

Numerous observations have been made at far-infrared, sub-millimeter and radio wavelengths. They all show that most of the emission at longer wavelengths originates from the optically obscured overlap region. From CO observations, Stanford et al. (1990) inferred that the total molecular gas mass in the overlap region is $1.2 \cdot 10^9 \mathrm{M}_\odot$, several times higher than the amount of gas in the two nuclei. For the entire Antennae system Gao et al. (2001) found a total molecular gas mass of $1.5 \cdot 10^{10} \mathrm{M}_\odot$, based on CO (1-0) observations. At the SFR of $\sim 20 \mathrm{M}_\odot\,\mathrm{yr}^{-1}$ derived by Zhang, Fall & Whitmore (2001), this leads to a gas consumption timescale of the order of 700 Myr. With high

resolution aperture synthesis CO maps from the Caltech Millimeter Array, the mass of individual star-forming regions was evaluated (Wilson et al. 2000). Masses of $(3-6)\cdot 10^8 M_\odot$ were found for the largest molecular complexes, which is typically an order of magnitude larger than the largest structures found in the disks of more quiescent spiral galaxies. The same paper reports an excellent correlation between the CO emission and the 15μm emission seen by ISO, as well as evidence for cloud-cloud collisions near the strongest mid-infrared peak.

Gao et al. (2001) estimate an average star formation efficiency (SFE) over the entire Antennae system of $L_{IR}/M_{H_2} \sim 4.2 L_\odot/M_\odot$, which is similar to that of GMCs in the Galactic disk, although some localized regions in the Antennae up to $L_{IR}/M_{H_2} \sim 20 L_\odot/M_\odot$ exist. Nikola et al. (1998) used the the Fabry-Perot interferometer FIFI aboard the Kuiper Airborne Observatory to map the [C II] line at 158 μm, which is the princopal of the PDRs. At an angular resolution of 55″ they found that the starburst in the Antennae is not global but confined to small regions of high star formation efficiency. Schulz et al. (2007) analyzed maps in ^{12}CO (1-0), (2-1), (3-2) and at 870μm, combined them with data from X-ray to radio, and applied them to PDR models. The modelled clouds have dense cores and low kinetic temperatures, showing no signs of intense starburst activity.

Observations with the VLA at 6 and 4 cm by Neff & Ulvestad (2000) yielded high resolution radio maps which became the basis for many subsequent studies.

X-ray observations at high angular resolution provided by Chandra revealed 49 sources, including several ultra-luminous X-ray (ULX) sources (Zezas et al. 2002a). A subsequent monitoring survey revealed ten ULXs, which show long-term variability (Zezas et al. 2006). These variations indicate that the ULXs are probably black hole/high mass X-ray binaries accreting via Roche lobe overflow. Feng & Kaaret (2006) speculated that the most luminous ULX, X-16, is a candidate for an intermediate mass black hole (IMBH). On the other hand, Zezas et al. (2007) argue that the strongest source has $L_X \sim 10^{40}\,\mathrm{erg\,s^{-1}}$, which could be produced by a $\sim 80 M_\odot$ black hole accreting at the Eddington limit. Clark et al. (2007) studied the infrared counterparts to the Chandra X-ray sources and found that the X-ray/IR matches are concentrated in the "spiral arms" and the overlap region, and hence are members of the SSCs, tracing the recent star formation history.

Based on spatially resolved spectra from Chandra ACIS-S, Baldi et al. (2006a) studied the hot interstellar medium (ISM) and found that the metal abundances for Ne, Mg, Si, and Fe vary throughout the ISM from $0.2 Z_\odot$ to $20-30 Z_\odot$. However, in their follow-up study Baldi et al. (2006b) found no correlation between the radio/optical star formation indicators and metallicity, assuming that supernovae (SNe) type II are the main contributors to metals in the hot ISM.

In this Chapter we study the central region of the Antennae galaxies based on spatially resolved mid-infrared spectroscopy. Our aim is to characterize the starburst activity in general, the super star clusters in particular, and their interplay (heating and ionization) with the interstellar medium. The outline of this Chapter is as follows: In the following Section we describe the observations along with the data reduction and calibration. In Section 5.3 we discuss how the spectral features have been measured and how the key parameters were derived. The main focus is on section 5.4, where we

discuss our numerous results, both on individual clusters and on the central region as a whole. This is followed by the summary in Section 5.5.

5.2 Observations and data reduction

We used the Infrared Spectrograph[1] (IRS) (Houck et al. 2004) on board the Spitzer Space Telescope (Werner et al. 2004) to observe the central interaction region of the Antennae galaxies at unprecedented depth. The IRS observations of the Antennae are part of a guaranteed time program (PI Houck, Spitzer PID 21) on the spectroscopic study of star formation in interacting galaxies. We have made observations in the two resolution modes of the IRS – 'hires' at $R = 600$ and 'lores' at $R = 65 - 130$ – using all four modules: Short-High (SH) [$9.9 - 19.6\mu$m], Long-High (LH) [$18.7 - 37.2\mu$m], Short-Low (SL) [$5.2 - 14.5\mu$m] and Long-Low (LL) [$14.0 - 38.0\mu$m]. The observing parameters are listed in Table 5.1 and described in more detail in Sections 5.2.1 and 5.2.2.

5.2.1 'Hires' observations

The spectra from the IRS 'hires' modules were taken with a standard staring mode Astronomical Observation Template, producing two exposures per 'cycle' at separate nod positions along the slit. The coordinates of the eight observed regions within NGC 4038/39 are listed in Table 5.2 and the slit positions are illustrated in Fig. 5.1. We note that the IRS position of the nucleus of NGC 4038 does not exactly coincide with the radio nucleus but is slightly shifted toward the north to also include the nearby, active star forming region.

Table 5.1 — Observing Parameters

	hires	lores
Obs.date	3 Jan 2005	3 Jul 2005
		12 Jul 2005
		23 Jan 2006
Pixel scale	2.″3 (SH)	1.″8 (SL)
	4.″5 (LH)	5.″1 (LL)
Slit size	4.″7 × 11.″3 (SH)	3.″6 × 57″ (SL)
	11.″1 × 22.″3 (LH)	10.″5 × 168″ (LL)
#[b] $\times t_{int}$	$12 \times 2 \times 30$s (SH)	2×14s (SL)
	$5 \times 2 \times 60$s (LH)	2×14s (LL)

[a] Astronomical Observing Request

[b] Number of exposures per position

The data were pre-processed by the *Spitzer* Science Center data reduction pipeline version 13.2 (Spitzer Observer's Manual, 2004). To avoid uncertainties introduced by the flat-fielding in earlier versions of the automated pipeline processing, we started from the two-dimensional, unflat-fielded data products. These products are part of the "basic calibrated data" (BCD) package provided by the *Spitzer* Science Center .

First, all images were cleaned of bad pixels using the IDL procedure *IRSCLEAN*. The various 2-dimensional spectra from the same nod position were median-combined

[1]The IRS was a collaborative venture between Cornell University and Ball Aerospace Corporation funded by NASA through the Jet Propulsion Laboratory and the Ames Research Center.

within the Spectral Modelling, Analysis, and Reduction Tool (*SMART*) version 5.5.1 (Higdon et al. 2004). A median 'sky' spectrum was computed from both nods of the sky position and subtracted from each median nod image. The spectral extraction was also done within *SMART*, using full aperture extraction, collapsing the full slit into a one-dimensional spectrum (slit sizes are listed in Table 5.1). The spectra were flat-fielded and flux calibrated by multiplication with the relative spectral response function (RSRF) using the IRS RSRF of the standard star ξ-Dra for both SH and LH spectra. We have not corrected for periodic "detector fringing" in the spectra since these artifacts have no effect on the analysis carried out in this Chapter.

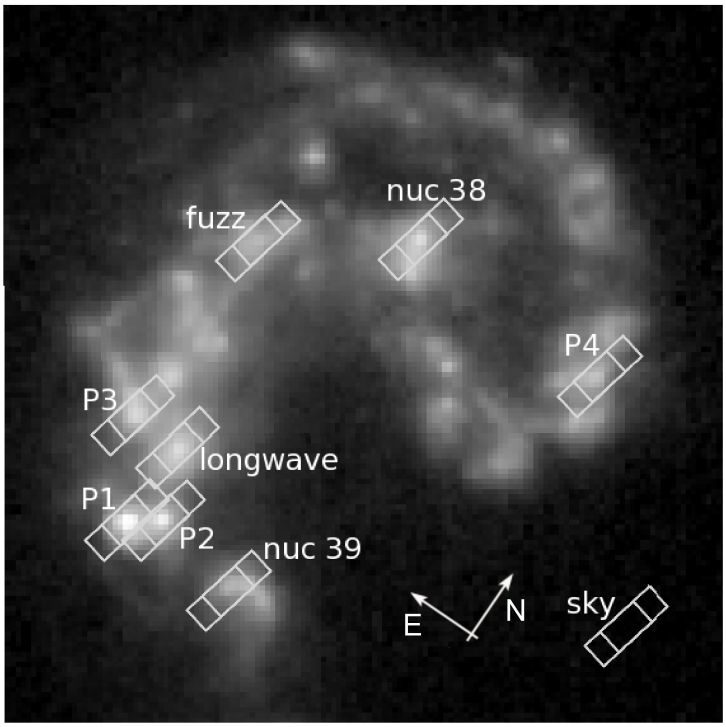

Figure 5.1 — The positions of the SH slits for the given observing date over-plotted on the IRAC 8μm map of the Antennae (Wang et al. 2004). The field size is 2.4 $\times$ 2.4 arcmin^2.

After these steps there was a noticeable and expected mismatch between the fluxes measured by the IRS SH and LH modules at the same wavelengths. Since this mismatch is most likely due to extended emission surrounding the regions of interest, picked up by the wider LH slit ($11\farcs1 \times 22\farcs3$ for the LH versus $4\farcs7 \times 11\farcs3$ for the SH slit), we scaled LH down to match SH. The scaling factors 'SF' applied to the LH fluxes are listed in Table 5.2. The resulting IRS 'hires' spectra from the two nuclei and the six infrared peaks are shown in Figs. 5.2, 5.3, and 5.4, respectively. The total observing time was 4.4 hours.

5.2.2 'Lores' observations

Observations were made with both 'lores' modules in spectral mapping mode. The AORs were intentionally designed to make use of the facts that the subslits SL1 and SL2 are adjacent and record data simultaneously, and that the orientation will have changed after six months (half a solar orbit). However, an unfortunate delay of six months in the scheduling doubled the spatial offset between SL1 and SL2 instead of providing the same spatial coverage. The problem was detected and corrected by requesting another SL1 map six months later, specifically designed to fill in the missing parts. The mapped areas are illustrated in Fig. 5.5. The total mapping time of all observations combined was 7.1 hours.

All data were processed with the standard pipeline version 13. Further reduction

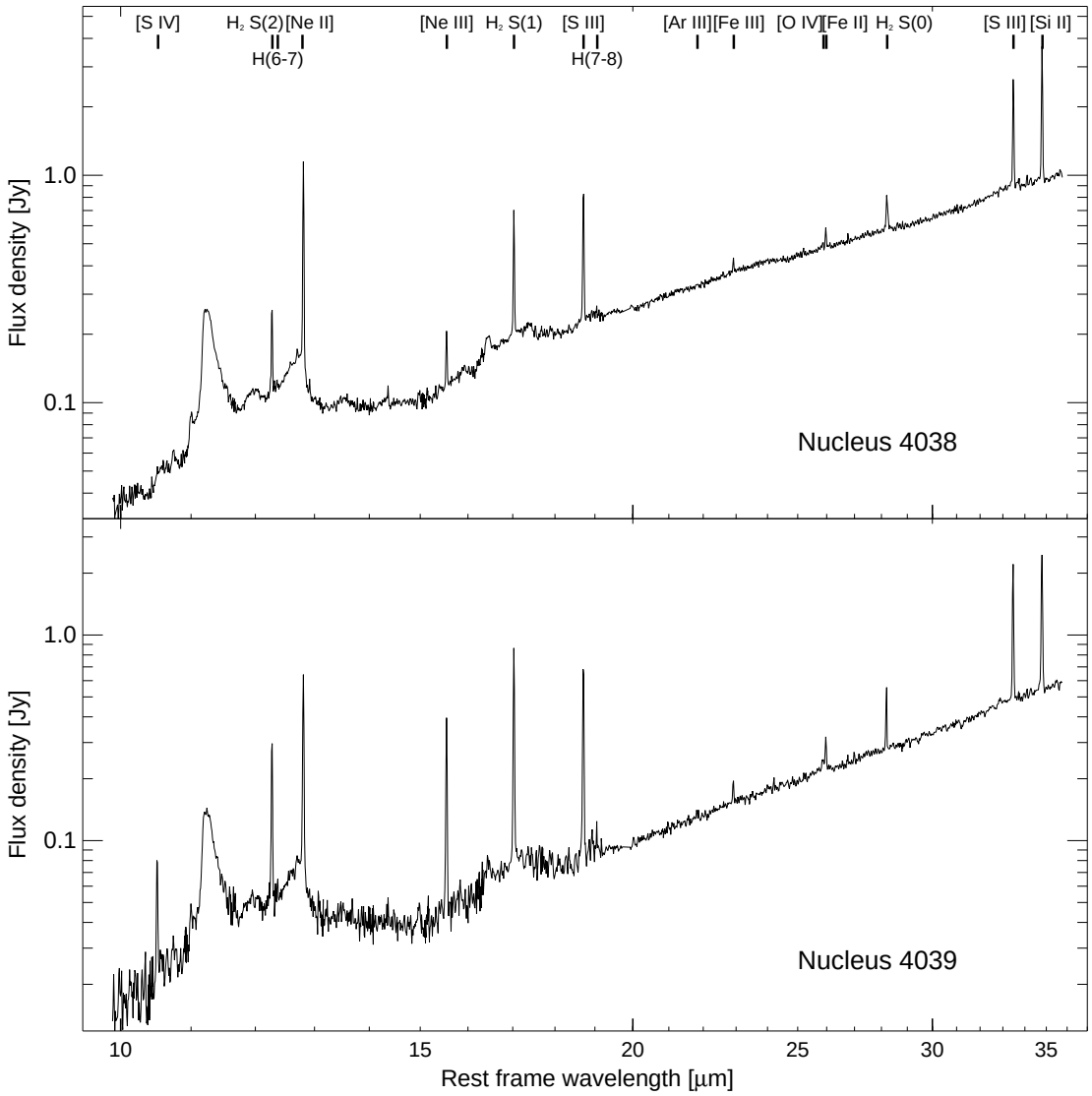

Figure 5.2 — IRS SH+LH spectra of the two nuclei of NGC 4038 (*top*) and NGC 4039 (*bottom*). The most prominent spectral lines are labelled.

and analysis started from the two-dimensional, flat-fielded data products, which are part of the BCD package provided by the Spitzer Science Center.

Most of the reduction and spectral analysis of the large data cube has been performed with *CUBISM* (Smith et al. 2006). *CUBISM* is an IDL program developed by the SINGS Legacy team to combine slit spectra at various angles and positions and create spectral maps and local spectra. However, the cubes built from the standard pipeline products showed numerous bright vertical stripes at many wavelengths due to pixels with artificially elevated flux values. Many of these pixels are located near the edges of the orders where the flat-field is less accurate. Various cleaning methods have been investigated to mitigate these artifacts. The best, although still not perfect results were obtained with a combination of a local noise estimate and median replacement, and the procedure *IRSCLEAN*, version 1.3. The latter is based on a multi-resolution analysis

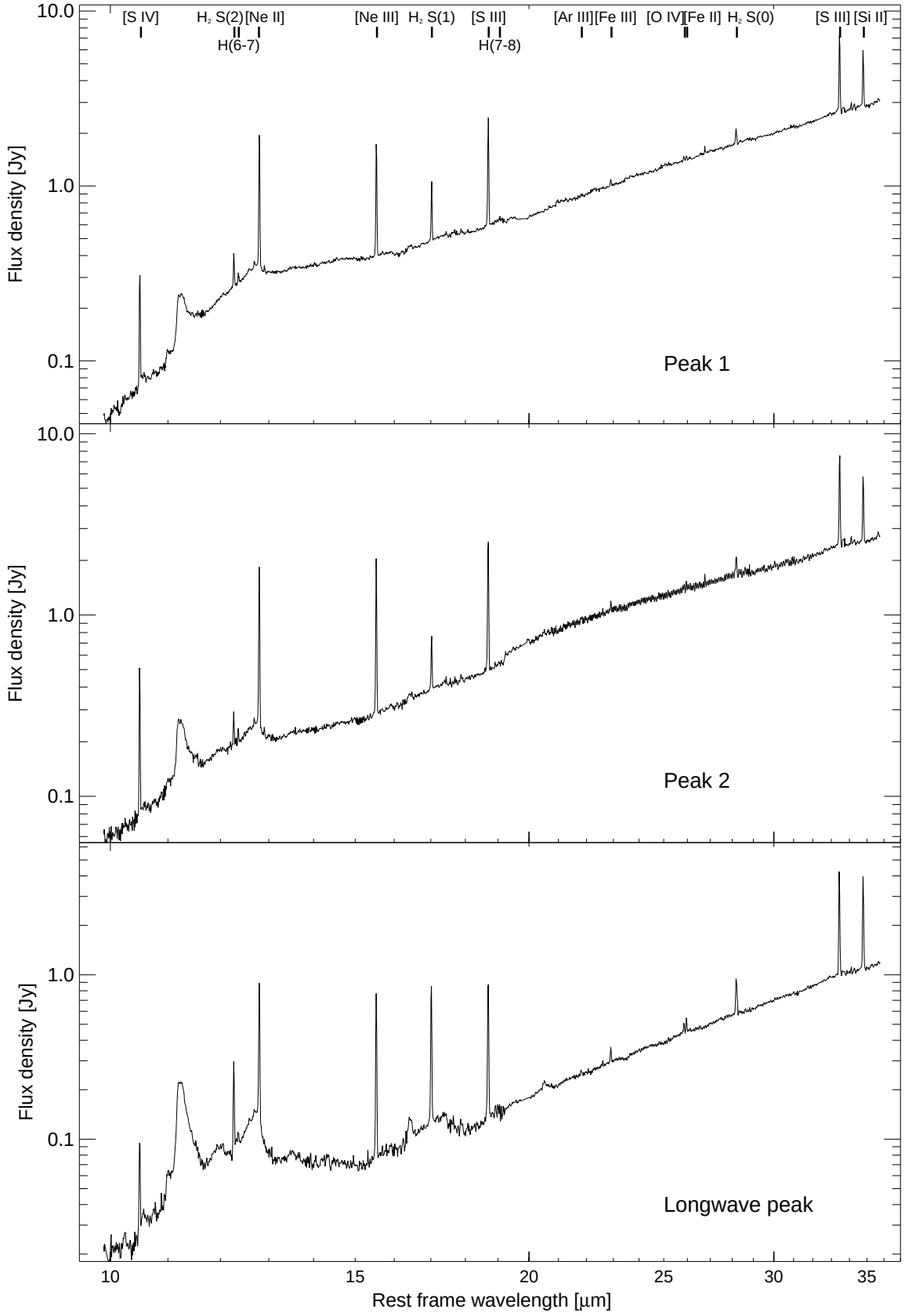

Figure 5.3 — IRS SH+LH spectra of the first three infrared peaks listed in Table 5.2 and illustrated in Fig. 5.1 (peak 1, 2, and longwave). The most prominent spectral lines are labelled.

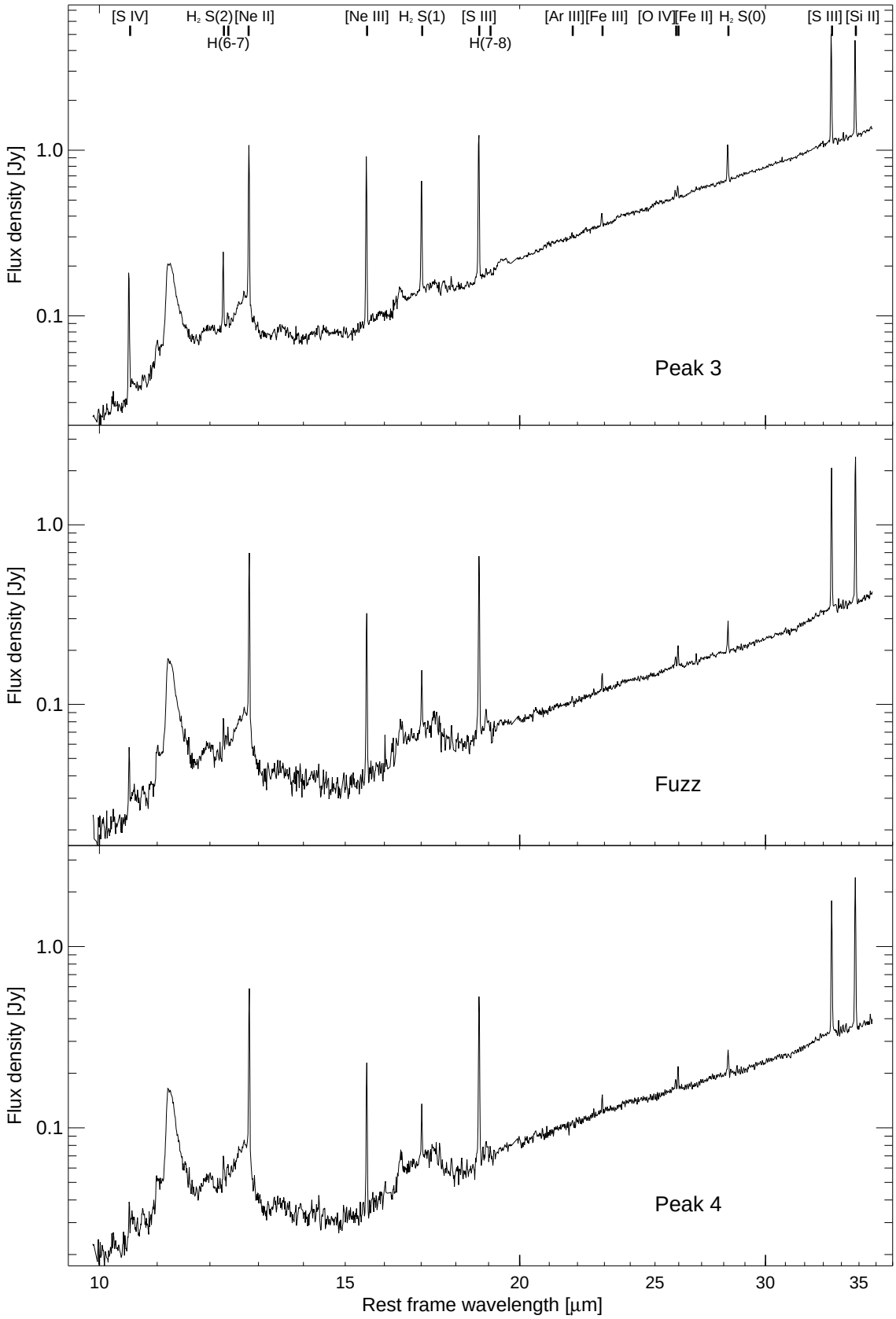

Figure 5.4 — As Fig. 5.3 for the last three clusters listed in Table 5.2 (peak 3, fuzz, and peak 4).

Table 5.2 — Parameters of the Pointed Observations with Cluster Designations from the Literature

Name	RA (J2000)	Dec (J2000)	LH SF[a]	WS95[b]	B05[c]	N00[d]
nucleus 4038	12 01 53.01	-18 52 02.7	0.77			
nucleus 4039	12 01 53.54	-18 53 10.2	0.63			
peak 1	12 01 54.98	-18 53 05.7	0.65	80	157	2-1
peak 2	12 01 54.58	-18 53 03.4	0.56	86(89/90)	136	2-6
longwave	12 01 54.75	-18 52 51.1	0.45	115	148	3-5
peak 3	12 01 55.39	-18 52 48.9	0.50	119/120(/117)	176	4-2
fuzz	12 01 54.80	-18 52 13.5	0.56	384/382/389	154	5-5
peak 4	12 01 50.42	-18 52 12.6	0.59	405	...	11-2
reference sky	12 01 49.00	-18 52 50.0				

[a] Scaling factor to multiply with the LH fluxes to match SH.

[b] WS95: optical imaging with the HST WF/PC (Whitmore & Schweizer 1995).

[c] B05: near-infrared imaging with Palomar WIRC (Brandl et al. 2005).

[d] N00: 4 and 6 cm radio observations with the VLA (Neff & Ulvestad 2000).

algorithm (Murtagh et al. 1995), where an image is subsequently smoothed to different scales, using a wavelet transform. *IRSCLEAN* is contributed IRS software, which we

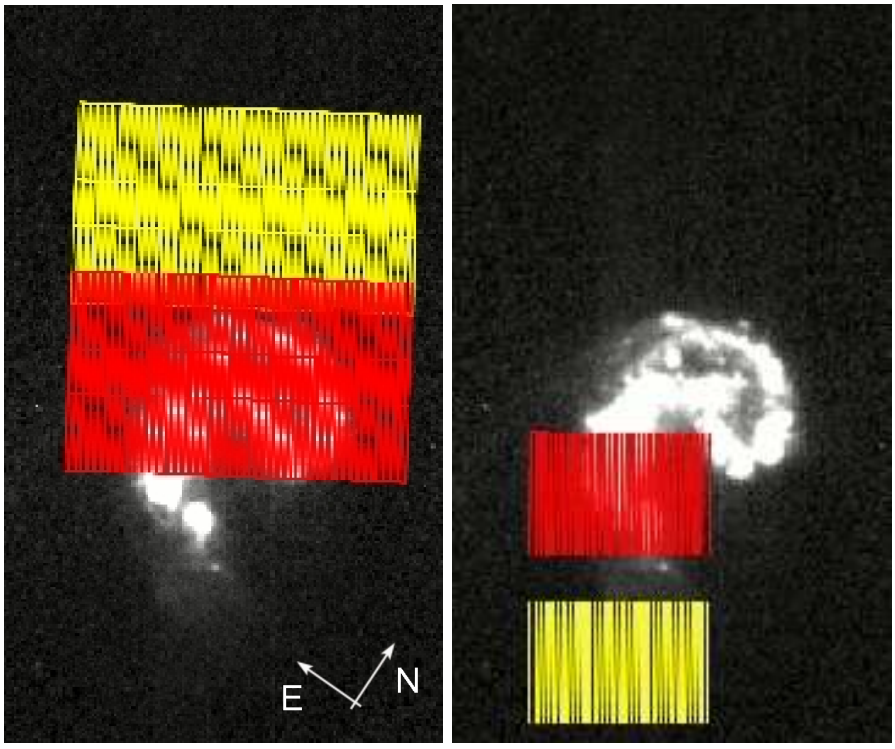

Figure 5.5 — Coverage of the IRS spectral map with SL1 (dark grey) and SL2 (light grey) over-plotted on the IRAC 8μm map of the Antennae (Wang et al. 2004). Left: the initial map. Right: the missing "filler" part. Both images approximately span 3.9×6.5 arcmin^2.

modified slightly to use a more localized noise estimate on a subslit basis. We have also used Gaussian rather than uniform noise estimates. Because the algorithm was applied first to "sky" spectra we are confident that this method did not accidentally remove spectral features of the sources.

Fig. 5.6 shows the resulting line maps for six important spectral features: the fine-structure lines of [Ne II] and [S IV], the molecular hydrogen H_2 S(2) and S(3) lines, and the 6.2 and 11.3μm emission features of polycyclic aromatic hydrocarbons (PAHs). More maps and a detailed discussion can be found in Section 5.4.

5.3 Results and methods

Figures 5.3, and 5.4 reveal the spectral richness of the high signal-to-noise spectra. Important common features include the PAH emission bands, ionic fine-structure lines, atomic and molecular hydrogen lines, and the spectral continuum. In this Section we describe how the quantities relevant to our discussion have been measured and how various properties were derived from the 'lores' and 'hires' spectra.

5.3.1 Continuum fluxes

In order to characterize the slope of the spectral continuum we have derived the flux densities at two wavelengths, namely at $14.75 - 15.25\mu$m and at $29.5 - 30.5\mu$m, here referred to as $F_{15\mu m}$ and $F_{30\mu m}$, respectively. These wavelengths have been chosen as they are not significantly affected by known emission or absorption features. This approach is similar to the one described in Brandl et al. (2006) and is arguably the best direct estimate of the spectral continuum. The flux measurements are listed in Table 5.3. The continuum fluxes will be discussed in detail in section 5.4.5.

Table 5.3 — Continuum Fluxes

Position	$F_{15\mu m}$ (mJy)	$F_{30\mu m}$ (mJy)	$F_{15\mu m}$ / $F_{30\mu m}$
nuc 4038	103 ± 10	649 ± 65	0.16 ± 0.02
nuc 4039	39 ± 4	334 ± 33	0.12 ± 0.02
peak 1	383 ± 38	1994 ± 199	0.19 ± 0.03
peak 2	260 ± 26	1853 ± 185	0.14 ± 0.02
longwave	69 ± 7	699 ± 70	0.10 ± 0.01
peak 3	79 ± 8	787 ± 79	0.10 ± 0.01
fuzz	35 ± 4	233 ± 23	0.15 ± 0.02
peak 4	32 ± 3	231 ± 23	0.14 ± 0.02

5.3.2 Polycyclic aromatic hydrocarbons (PAHs)

The spectra in Figs. 5.3 and 5.4 show that the spectral shape at the short wavelength side is largely dominated by the strong emission features from PAHs. Here we describe the methods used to determine their strengths and the uncertainties involved.

The strengths and equivalent widths of the PAH features were measured using the IDL program *PAHFIT* (Smith et al. 2007). *PAHFIT* decomposes the spectra into the individual contributions from starlight, thermal emission from dust, atomic and

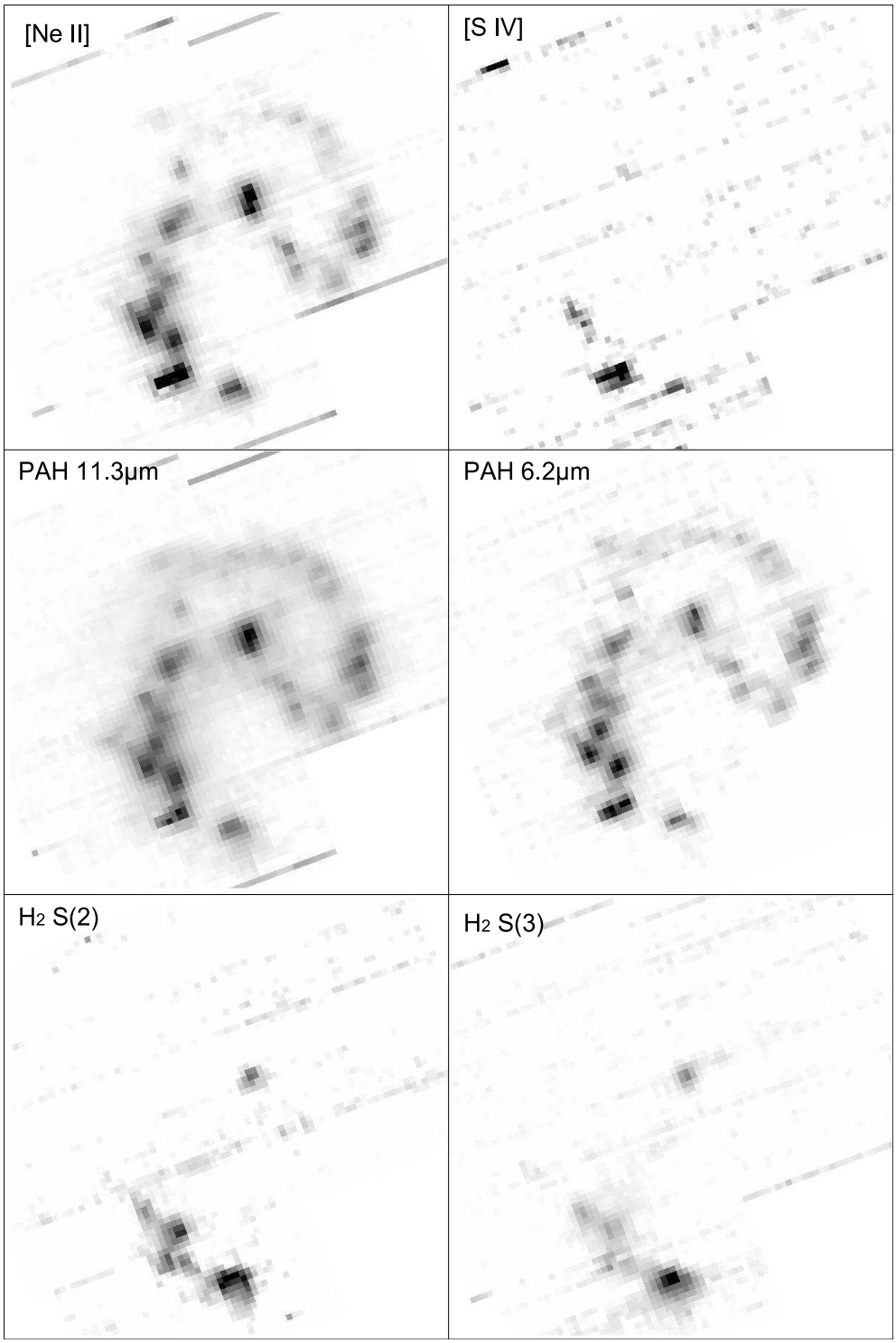

Figure 5.6 — IRS-SL spectral maps of the [Ne II] and [S IV] lines (top), the 11.3μm and 6.2μm PAH features (center), and the S(2) and S(3) rotational lines of H_2. The spectral continuum has been subtracted and the images shown represent the pure line intensities; hence the signal-to-noise can be very low at certain wavelengths or image positions. All maps are shown in linear scaling. North is up, east is left. All panels span 2.8 $\times$ 2.8 arcmin^2. For a discussion see section 5.4.4

molecular emission lines, and the PAH emission bands. The latter, combined with extinction dominated by the silicate absorption bands around 9.7 and 18μm, is the main application of the routine and both are treated meticulously. Since *PAHFIT* has been designed to analyze IRS 'lores' spectra and does not accurately fit narrow emission lines we removed the emission lines from the 'hires' spectra for the purpose of the PAH measurements. This was done by linear interpolation between the fluxes directly shortwards and longwards of the emission lines. *PAHFIT* uses Drude profiles to fit 15 PAH features of different width in the IRS-SH range.

The starlight is modelled by the default 5000 K continuum blackbody, resulting in a relatively small contribution to the spectrum in some cases (less than 25% at 10μm and less than 10% longwards of 11μm for peak 1, 2 and 3) and a significant contribution to the short wavelength part of the spectrum in others ($\approx$ 100% at 10μm, dropping below 10% around 18μm in the case of peak 4, fuzz, longwave and the nucleus of 4038). The spectrum of the nucleus of NGC 4039 lies somewhere in between these extreme cases.

The thermal dust continuum is fitted by a combination of modified black bodies at fixed temperatures of 35, 40, 50, 90, 135, 200 and 300 Kelvin. *PAHFIT* can automatically correct for extinction estimated from the depth of the 9.7μm silicate absorption feature. However, we have turned off this automatic feature since the 'hires' spectra cover only part of the 9.7μm silicate absorption and we noticed that, under these conditions, extinction is being used as a free parameter to optimize fit results without strong physical motivation.

The central wavelength of the PAH features was fixed and the Full Width at Half Maximum (FWHM) was allowed to vary by at most 20%. Several adjacent, broad PAH features could not be resolved and are blended into one broad complex, and we list the combined fluxes from both components. Such cases are the features at 11.23 and 11.33μm, and at 12.62 and 12.69μm. The PAH features at 14.04, 15.9, 18.92 and 33.1μm were not included in the analysis because of their intrinsic weakness and large systematic uncertainties. The measured PAH fluxes and equivalent widths are listed in Table 5.4. The listed uncertainties include the uncertainty in the absolute flux calibration, which we estimate to be of the order of 10%, and the fit error as given by *PAHFIT*. Both contributions have been added in quadrature. The measurements for 'peak 1' are not included in the table since the fit results were obviously inaccurate. The PAH features are intrinsically weak in 'peak 1', but *PAHFIT* approximated the continuum emission by a linear combination of very strong emission features with obviously incorrect results longward of 13μm. The fits to all other spectra appear to be accurate.

The PAH strength in the 'lores' spectra has been visualized and analyzed within *CUBISM* in a more qualitative way. We co-added the emission from the spectral elements covered under the emission feature and subtracted the continuum flux. The latter was derived from a linear interpolation between the continuum short- and longward of the emission feature. The short- and longward continuum fluxes were the median of typically three spectral resolution elements.

We produced spectral maps in the 6.2μm, 8.6μm and 11.3μm PAH emission features, not all of which are presented in this Chapter. Although the signal-to-noise of the 8.6μm map is lower than that of the 11.3μm PAH map the systematic uncertainties for the latter are higher, being most sensitive to the silicate absorption band. Since

Table 5.4 — PAH feature strengths longward of 10μm[a]

Position[d]	$F_{10.7\mu m}$[b] $EW_{10.7\mu m}$[c]	$F_{11.3\mu m}$[b] $EW_{11.3\mu m}$[c]	$F_{12.0\mu m}$[b] $EW_{12.0\mu m}$[c]	$F_{12.7\mu m}$[b] $EW_{12.7\mu m}$[c]	$F_{13.5\mu m}$[b] $EW_{13.5\mu m}$[c]
nuc 4038	0.73 ± 0.40	18.02 ± 1.40	9.41 ± 0.65	14.24 ± 1.36	3.89 ± 0.46
	0.05 ± 0.03	1.31 ± 0.15	0.67 ± 0.08	0.97 ± 0.14	0.24 ± 0.04
nuc 4039	0.53 ± 0.09	9.91 ± 0.69	4.45 ± 0.25	7.17 ± 0.59	1.97 ± 0.18
	0.09 ± 0.02	1.70 ± 0.19	0.75 ± 0.09	1.18 ± 0.16	0.31 ± 0.04
peak 2	0.67 ± 0.25	14.41 ± 1.57	9.54 ± 0.77	17.54 ± 1.98	7.57 ± 0.76
	0.02 ± 0.01	0.47 ± 0.02	0.28 ± 0.04	0.48 ± 0.08	0.19 ± 0.03
longwave	0.36 ± 0.19	15.57 ± 0.80	7.06 ± 0.84	14.25 ± 1.11	4.07 ± 0.28
	0.04 ± 0.01	1.79 ± 0.21	0.75 ± 0.08	1.40 ± 0.18	0.37 ± 0.05
peak 3	0.40 ± 0.11	13.67 ± 0.69	6.42 ± 0.34	11.09 ± 0.95	3.30 ± 0.28
	0.04 ± 0.01	1.24 ± 0.14	0.56 ± 0.06	0.92 ± 0.12	0.26 ± 0.03
fuzz	0.70 ± 0.08	12.97 ± 0.85	4.18 ± 0.58	9.00 ± 1.17	1.66 ± 0.30
	0.10 ± 0.02	2.00 ± 0.23	0.70 ± 0.08	1.56 ± 0.23	0.29 ± 0.04
peak 4	0.68 ± 0.09	12.17 ± 0.82	4.02 ± 0.56	8.12 ± 1.07	1.42 ± 0.29
	0.10 ± 0.02	2.06 ± 0.23	0.75 ± 0.09	1.60 ± 0.24	0.28 ± 0.04

Position[d]	$F_{14.2\mu m}$[b] $EW_{14.2\mu m}$[c]	$F_{16.5\mu m}$[b] $EW_{16.5\mu m}$[c]	$F_{17.4\mu m}$[b] $EW_{17.4\mu m}$[c]	$F_{17.9\mu m}$[b] $EW_{17.9\mu m}$[c]
nuc 4038	1.20 ± 0.24	1.27 ± 0.20	6.80 ± 1.40	0.46 ± 0.63
	0.07 ± 0.02	0.06 ± 0.01	0.29 ± 0.04	0.02 ± 0.01
nuc 4039	6.06 ± 0.10	0.51 ± 0.08	3.53 ± 0.36	0.30 ± 0.10
	0.09 ± 0.02	0.06 ± 0.01	0.42 ± 0.06	0.03 ± 0.01
peak 2	3.10 ± 0.53	0.29 ± 0.36	...	...
	0.07 ± 0.01	0.01 ± 0.01	...	...
longwave	1.46 ± 0.18	0.90 ± 0.13	4.03 ± 0.78	...
	0.13 ± 0.02	0.06 ± 0.01	0.27 ± 0.05	...
peak 3	0.90 ± 0.19	0.90 ± 0.15	3.39 ± 0.95	...
	0.07 ± 0.02	0.05 ± 0.01	0.18 ± 0.04	...
fuzz	0.96 ± 0.11	0.79 ± 0.09	3.67 ± 0.77	...
	0.16 ± 0.02	0.11 ± 0.02	0.50 ± 0.05	...
peak 4	0.67 ± 0.13	0.58 ± 0.07	3.43 ± 0.40	...
	0.13 ± 0.03	0.09 ± 0.01	0.49 ± 0.07	...

[a] All measured in the SH slit, covering $4\farcs7 \times 11\farcs3$

[b] Flux in units of 10^{-13}erg sec^{-1} cm^{-2}

[c] Equivalent width in units of μm

[d] Position 'peak 1' is not included in this table since *PAHFIT* did not yield reliable fit results (see main text for details).

the 12.7μm PAH map may be affected by the strong [Ne II] line at 12.81μm we did not include it in the further analysis. The 6.2μm and 11.3μm PAH maps are shown in Fig. 5.6.

5.3.3 Fine-structure and hydrogen emission lines

As can be seen in Figs. 5.2, 5.3, and 5.4 the $5 - 38\mu$m wavelength range contains numerous strong fine-structure emission lines, most prominently from sulphur and neon. We measured the line fluxes from the 'hires' spectra using the Gaussian line fitting tool in *SMART* and a linear baseline fit. The results are listed in Table 5.5. The quoted uncertainties include the uncertainty in the absolute flux calibration, which we estimate to be in the order of 10%, and the fit errors provided by *SMART*. Both contributions have been added in quadrature.

Our measurements of [Ne III]/[Ne II] are in the range of $0.08 - 0.75$, and hence lower than the[Ne III]/[Ne II] ~ 0.8 derived by Kunze et al. (1996) with ISO-SWS spectroscopy for the overlap region. However, our "line-luminosity weighted" average value for the peaks 1, 2, 3, longwave and fuzz together is $0.57^{+0.13}_{-0.11}$, still lower than but close to the ISO-SWS value of 0.8.

Figs. 5.2, 5.3, and 5.4 also show the lowest pure rotational transitions of molecular hydrogen, namely the 0-0 S(0) 28.21μm, the 0-0 S(1) 17.03μm, and the 0-0 S(2) 12.28μm lines. In addition, we find the atomic hydrogen lines H I (7-6) 12.37μm and the H I (8-7) 19.06μm. The latter, however, has only been detected in the nucleus of NGC 4039. The line fluxes are listed in Table 5.7. The quoted uncertainties include the uncertainty in the absolute flux calibration, which we estimate to be in the order of 10%, and the fit errors provided by *SMART*. Both contributions have been added in quadrature.

The line strength in the 'lores' spectra has been visualized and analyzed with *CUBISM* in the same way as the PAH features before. We concentrate the analysis on the strongest fine-structure and hydrogen lines within the range of the IRS-SL module in order to have similar spatial resolution for all maps (the slit width increases by a factor of two longward of 15μm.) Hence, we present the [S IV] map in Fig. 5.6 instead of [Ne III] which lies outside the range covered by the IRS-SL module.

The measurement of the [Ne II] line at 12.81μm is slightly hampered by the 12.7μm PAH emission feature in 'lores' mode. A cross-contamination may lead to an overestimation of the line flux, but also to an overestimation of the continuum flux. For that reason we have excluded the 12.7μm PAH feature from our analysis. A comparison of the [Ne II] line flux in the nucleus of NGC 4039 with the 'hires' spectrum, where the components are clearly resolved, indicates that the PAH contamination to the line flux is small, of the order of $\leq 10\%$.

The 0-0 S(1)17.03μm, the 0-0 S(2)12.28μm and the 0-0 S(3)9.66μm emission lines of molecular hydrogen were also detected in the 'lores' spectral maps. The S(2) and S(3) lines were both measured with the IRS-SL1 module, while the S(1) line was measured with the IRS-LL2 module at $\sim 2\times$ lower spatial resolution. The fluxes of the S(2) and S(3) lines derived from the IRS-SL spectral map for our distinct pointings have been added to Table 5.7. Fig. 5.6 shows the spectral maps at the [Ne II], [S IV], and the H_2 0-0 S(3)9.66μm lines.

Table 5.5 — Fine-structure line fluxes in units of 10^{-13}erg sec^{-1} cm^{-2}

Position	[S IV][a] 10.51μm	[Ne II][a] 12.81μm	[Ne III][a] 15.56μm	[S III][a] 18.71μm	[Ar III][b] 21.83μm
nuc 4038	...	3.83 ± 0.40	0.29 ± 0.03	1.89 ± 0.20	...
nuc 4039	0.34 ± 0.04	2.41 ± 0.25	1.14 ± 0.12	1.91 ± 0.20	...
peak 1	1.25 ± 0.14	7.05 ± 0.77	4.44 ± 0.46	5.14 ± 0.52	0.05 ± 0.08
peak 2	1.87 ± 0.19	6.64 ± 0.70	4.86 ± 0.49	6.22 ± 0.69	...
longwave	0.39 ± 0.04	3.33 ± 0.34	2.31 ± 0.23	2.43 ± 0.25	0.05 ± 0.02
peak 3	0.78 ± 0.08	3.98 ± 0.41	2.48 ± 0.26	3.21 ± 0.32	...
fuzz	0.14 ± 0.02	2.47 ± 0.27	0.95 ± 0.10	1.71 ± 0.18	0.02 ± 0.00
peak 4	0.05 ± 0.01	2.11 ± 0.25	0.65 ± 0.07	1.37 ± 0.14	...

Position	[Fe III][b] 22.93μm	[O IV][b] 25.89μm	[Fe II][b] 25.99μm	[S III][b] 33.48μm	[Si II][b] 34.82μm
nuc 4038	0.12 ± 0.02	0.12 ± 0.04	0.21 ± 0.03	2.75 ± 0.28	3.88 ± 0.39
nuc 4039	0.11 ± 0.01	0.10 ± 0.69	0.23 ± 0.31	2.67 ± 0.27	3.25 ± 0.33
peak 1	0.22 ± 0.04	0.14 ± 0.03	0.16 ± 0.04	7.64 ± 0.80	4.73 ± 0.51
peak 2	0.30 ± 0.09	...	0.26 ± 0.14	8.72 ± 0.93	5.19 ± 0.54
longwave	0.17 ± 0.02	0.17 ± 0.04	0.22 ± 0.02	5.14 ± 0.53	4.51 ± 0.46
peak 3	0.18 ± 0.02	0.13 ± 0.02	0.21 ± 0.03	6.09 ± 0.62	4.90 ± 0.50
fuzz	0.07 ± 0.01	0.06 ± 0.01	0.10 ± 0.01	2.55 ± 0.26	3.23 ± 0.33
peak 4	0.06 ± 0.01	0.05 ± 0.01	0.10 ± 0.01	3.18 ± 0.32	3.18 ± 0.32

[a] Measured in the SH slit, covering $4\farcs7 \times 11\farcs3$

[b] Measured in the LH slit, covering $11\farcs1 \times 22\farcs3$, though scaled down to match the LH part of the spectrum match the SH part (see explanation in Section 5.2.1)

5.3.4 Deriving H_2 temperatures and masses

The H_2 lines serve as crucial diagnostics of the conditions of the ISM. Here we outline how the temperatures and masses were calculated from the line fluxes. All the observable lines at mid-infrared wavelengths originate from quadrupole rotational transitions. The rotational levels of H_2 can be populated in various ways: H_2 molecules may already form in an excited state (Takahashi 2001); X-ray photons from energetic sources like AGN or supernova remnants can ionize and heat the gas, which excites the H_2 molecules via collisions with electrons and/or hydrogen atoms (Lepp & McCray 1983; Draine & Woods 1992); FUV photons can pump the H_2 molecules into excited states (Black & van Dishoeck 1987; Hollenbach & Tielens 1997); and the excitation via shocks in the ISM (Draine et al 1983; Shull & Hollenbach 1978). In starburst environments we can neglect the former two scenarios and concentrate on UV pumping and shocks. Both have been shown to play a dominant role in the excitation of H_2 in star-

burst environments (e.g., Moorwood & Oliva 1994; Roussel et al. 2007, and references therein).

UV pumping requires photons with energies $E_\gamma = 6 - 13.6\,\mathrm{eV}$ to electronically excite the H_2 molecules, which can relax via a cascade of vibration-rotational levels, producing characteristic fluorescent spectra. Shock heating can also play a significant role. On small scales, stellar outflows and supernova remnants can excite H_2 (Shull & Hollenbach 1978). On larger, galactic scales, streaming motions and cloud-cloud collisions, in particular in merging systems have been proposed (Van der Werf et al. 1993; Gilbert et al. 2000; Haas et al. 2005). Pure fluorescent spectra can usually be distinguished from thermalized, shock heated spectra from the relative line strengths. However, depending on the densities, in case of UV fluorescence collisional de-excitation can also become important for vibrational H_2 states, leading to thermalized lower levels. This mainly affects the S(0) to S(2) rotational levels where the critical densities are rather low, of the order of $\sim 10^3\,\mathrm{cm}^{-3}$. Most of the emission of warm H_2 is likely to come from dense PDRs with densities $\geq 10^3\,\mathrm{cm}^{-3}$ (Chapter 4), and we expect the observed S(0) through S(3) lines to be thermalized (Burton et al. 1992).

The H_2 molecule exists in two states: ortho-H_2 with parallel nuclear spins (odd J), and para-H_2 with anti-parallel spins (even J). The ortho-para ratio is normally assumed to be 3, which is the ratio of the statistical weights. The S(0) and S(2) lines are from para-H_2, while the S(1) and S(3) lines are from ortho-H_2. Hence, the line ratios of the same "species" are independent of the ortho-to-para ratio while the ratio of two lines adjacent in wavelength is sensitive to the ortho-to-para ratio. Generally, lines of transitions with higher energy levels probe also higher excitation temperatures. Unfortunately, we have to use a mixture of ortho and para lines for observational reasons: a reasonable comparison can only be done for lines observed with the same IRS module (slit width). Hence, our analysis of the "lores" maps will focus on the S(2) and S(3) lines, and the "hires" spectra on the S(1) and S(2) lines.

In the following calculations we assume that the observed line emission is optically thin, the critical densities of the observed levels are $n_{cr} \leq 10^3\,\mathrm{cm}^{-3}$ (this is certainly given for the S(0) through S(2) lines), that the levels involved are thermalized, and that the populated levels are in LTE with an ortho-to-para ratio of 3. The S-level refers to transitions with $\Delta J = J_{upper} - J_{lower} = +2$, and with $g_J = g_s(2J+1)$ (see Table 5.6). g_s is the nuclear statistical weight factor, which is 1 for para and 3 for ortho H_2.

Table 5.6 — H_2 molecular data

λ (μm)		J_{upper}	$g_{J,upper}$	E_u/k (K)	A_{ul}[a] (s^{-1})
28.219	S(0)	2	5	509.9	$2.94 \cdot 10^{-11}$
17.035	S(1)	3	21	1015.1	$4.76 \cdot 10^{-10}$
12.279	S(2)	4	9	1681.7	$2.76 \cdot 10^{-9}$
9.665	S(3)	5	33	2503.8	$9.84 \cdot 10^{-9}$

[a] The upper-level energies E_u and Einstein A coefficients A_{ul} were taken from Rosenthal et al. (2000) and references therein. g_J is the level degeneracy of rotational level J.

In order to derive the excitation temperature T_{ex} we apply the following calculation:

the column density N_i for a given level i is related to the total column density N_{tot} via the Boltzmann distribution:

$$\frac{N_i}{N_{tot}} = \frac{g_i}{Z_{H_2}(T)} e^{\frac{-E_i}{kT}}, \tag{5.1}$$

where $Z_{H_2}(T)$ is the temperature-dependent partition function of H_2, and g_i is the level degeneracy of level i. $Z_{H_2}(T)$ is defined as $\sum_J g_J \exp\left[-E_J/kT\right]$. Hence, the ratio of two level populations is

$$\frac{N_1}{N_2} = \frac{g_1}{g_2} e^{\left[\frac{E_2-E_1}{kT}\right]}. \tag{5.2}$$

The intensity of line I_i is related to the column density via

$$N_i = \frac{4\pi\lambda}{hc}\frac{I_i}{A_i}, \tag{5.3}$$

and the Einstein coefficient A_i describes the spontaneous emission probability. Thus the excitation temperature T_{ex} can be calculated as

$$T_{ex} = \frac{E_2 - E_1}{k \ln\left(\frac{g_2}{g_1}\frac{\lambda_1}{\lambda_2}\frac{I_1}{I_2}\frac{A_2}{A_1}\right)}. \tag{5.4}$$

The temperatures were calculated independently for the 'lores' and the 'hires' data and are listed in Table 5.10 and range from approximately 270 K to 370 K. We emphasize that the two independent temperature estimates using different lines and different

Table 5.7 — Line fluxes of molecular and atomic hydrogen in units of 10^{-13}erg sec^{-1} cm^{-2} observed in the IRS-SL and -SH modules

Position	$H_2S(3)$[a] 9.67μm	$H_2S(2)$[a] 12.28μm	$H_2S(2)$[b] 12.28μm	$H_2S(1)$[b] 17.03μm	$H_2S(0)$[c] 28.22μm	H (7-6)[b] 12.37μm
nuc 4038	0.74 ± 0.08	0.51 ± 0.06	0.64 ± 0.08	1.43 ± 0.15	0.72 ± 0.21	0.06 ± 0.01
nuc 4039	3.82 ± 0.38	2.13 ± 0.22	1.11 ± 0.12	2.37 ± 0.24	0.43 ± 0.08	0.04 ± 0.05
peak 1	≤ 0.50[d]	0.44 ± 0.05	0.62 ± 0.08	1.64 ± 0.17	0.81 ± 0.09	0.15 ± 0.02
peak 2	0.53 ± 0.06	0.50 ± 0.06	0.36 ± 0.06	1.23 ± 0.13	1.09 ± 0.24	0.11 ± 0.04
longwave	0.70 ± 0.07	0.72 ± 0.08	0.95 ± 0.11	2.38 ± 0.24	0.87 ± 0.10	0.11 ± 0.02
peak 3	0.52 ± 0.06	0.45 ± 0.05	0.66 ± 0.07	1.77 ± 0.18	0.90 ± 0.10	0.11 ± 0.03
fuzz	...	...	0.13 ± 0.03	0.24 ± 0.03	0.16 ± 0.02	0.05 ± 0.01
peak 4	...	...	0.11 ± 0.03	0.19 ± 0.02	0.22 ± 0.05	0.06 ± 0.02

[a] Observed with the IRS-SL module. Note that the quoted uncertainties include the fitting and photometric uncertainties but not systematic errors of the spectral mapping

[b] Observed with the IRS-SH module ($4\farcs7 \times 11\farcs3$). The H (8-7) line at 19.06μm was only measured in the spectrum of nuc 4039 with a line flux of $0.05 \pm 0.01 \cdot 10^{-13}$erg sec^{-1} cm^{-2}.

[c] Observed with the IRS-SH module ($11\farcs1 \times 22\farcs3$), though scaled down to match the LH part of the spectrum match the SH part (see explanation in Section 5.2.1)

[d] Upper limit due to an artifact in the spectral map.

measurements from different instruments agree remarkably well, to better than 10%. This is likely because the individual spectra are dominated by single sources which almost completely thermalize the warm H_2.

In order to derive the mass of warm H_2 we use the following calculation: for an ortho-to-para ratio of 3 the total mass of H_2 is $M_{H_2} = \frac{4}{3} M_{ortho} = \frac{4}{3} m_{H_2} N_{H_2}$, where m_{H_2} is the molecular mass of hydrogen, and the total number of molecules is

$$N_{H_2} = \frac{4\pi D^2 \lambda F}{hc A_{ul} N_i}. \tag{5.5}$$

F is the detected line flux and Ni describes the fractional population in the upper level as in Equation 5.1. For the temperature range between $250 - 400\,\mathrm{K}$, Z_{H_2} varies from 6 to 10. Combining the above equations we get

$$M_{H_2} = \frac{16\pi}{3} \frac{m_{H_2} D^2 \lambda F Q_{H_2}}{hc A_{ul} g_J \exp\left[-E_J/kT\right]}. \tag{5.6}$$

The H_2 masses were calculated independently for the 'lores' and the 'hires' data and are listed in Table 5.10 and discussed in Section 5.4.9.

Table 5.10 does not list the uncertainties in the temperature and mass estimates because they are dominated by three components, which we discuss here. First, there are the errors in the line flux measurements and listed in Table 5.5. They are typically between 10 and 15%. Second, the different clusters suffer different amounts of extinction. Correcting for extinction has two effects: it increases the line fluxes and it changes the line ratios. For instance, a "typical" optical depth of $\tau_{9.7} = 0.2$ would raise the temperature determined from the S(2) and S(3) lines by about 4% ($\sim 12\,\mathrm{K}$) since the S(3) is located in the center of the silicate band and suffers most from extinction. If we use the S(1) and S(2) lines instead, the temperatures rises only by 0.7% ($\sim 2\,\mathrm{K}$). The effect of extinction on the mass estimate is more subtle since the mass increases linearly with the corrected line flux but depends also on the temperature. For $\tau_{9.7} = 0.2$ the H_2 mass increases by approximately 5%. Given the large uncertainties in the A_V or $\tau_{9.7}$ for the clusters, as discussed in Section 5.3.5 and summarized in Table 5.8, we decided not to correct our tabulated estimates for extinction. Third, aperture effects play an important role. The 'hires' aperture is defined by the slit width and length and not matched to the size of the H_2 emitting region. This is not a problem for point sources but it is for extended regions such as the nucleus of NGC 4039. For the 'lores' values the aperture was matched to the size of the region. This systematic error is reflected in Table 5.10 by the difference between the corresponding mass estimates, and is the dominating uncertainty.

5.3.5 Extinction estimates

Although extinction at mid-infrared wavelengths is generally more than an order of magnitude less than at optical wavelengths, it may become important for the study of the more embedded cluster population. The wavelength range covered by the IRS-SL and SH modules includes two important diagnostics to estimate the amount of dust:

a broad Si=O stretching resonance, peaking at 9.7μm, and an even broader O-Si-O bending mode resonance, peaking at 18.5μm. We have estimated the extinction using two independent methods: via *PAHFIT* and via continuum baseline interpolation at the 9.7μm absorption feature.

The working method of *PAHFIT* was briefly summarized in section 5.3.2. We ran *PAHFIT* to derive the extinction values from the IRS-SH spectra of the six positions. The results are listed in Table 5.8. However, we did not use the *PAHFIT* default setting to automatically correct the measurements for extinction, and hence the values in Table 5.4 (and Table 5.5) are the directly measured fluxes which have not been corrected for extinction. This has been done for two reasons. First, *PAHFIT* has many free parameters, and given the limited spectral range of the IRS-SH module, which does not fully cover the 9.7μm silicate band, extinction would be used as yet another free parameter to optimize the overall fit. Second, the extinction is generally rather low in these objects and does not play a significant role at mid-infrared wavelengths, except for the most heavily obscured source, peak 1, which shows the strongest dust absorption features.

Our second, independent, method is based on the apparent optical depth in the 9.7μm silicate feature, directly measured as the natural logarithm of the ratio of observed flux to the nominal mid-infrared continuum at 9.7μm. The latter can be best estimated (for PAH dominated spectra) by a power law fit anchored at 5.5μm and 14.5μm. The method is described and illustrated in Fig. 2 of Spoon et al. (2007).

For a statistically large sample of 172 near-infrared sources in the Antennae, Brandl et al. (2005) found that the average extinction is about $A_V \sim 2$, while the reddest clusters may be reddened by up to 10 magnitudes. These and other values from the literature are compared with our measurements, and with the values for the extinction that were presented in Chapter 4 (Table 5.8). Because the IRS-SH spectra do not fully cover the 9.7μm silicate band, we regard the *PAHFIT*-derived extinction estimates as upper limits. With the exception of 'longwave', both methods yield values that are proportional to each other, albeit the *PAHFIT* upper limits are on average a factor five larger. The conversion from $\tau_{9.7}$ to A_V strongly depends on the assumed extinction law. Toward the Galactic Center there are various estimates: $A_V/\tau_{9.7} \sim 6.7$ (Moneti et al. 2001), $A_V/\tau_{9.7} \sim 7.8$ (Lutz 1999), and $A_V/\tau_{9.7} \sim 9.0$ (Mathis 1990). For the Solar neighbourhood Mathis (1990) derived $A_V/\tau_{9.7} \sim 18.5$), and Draine (1989) calculated $A_V/\tau_{9.7} \sim 18.1$. Given this broad range of conversion factors, we find that the estimates for $\tau_{9.7}$ from baseline fitting agree resonably well with the other values listed in Table 5.8, except for those for peak 1. The values found for $\tau_{9.7}$ indicate less extinction than derived from observations at shorter wavelengths. Furthermore, the ratio of $A_V/\tau_{9.7}$ is significantly different for the individual sources. This and the low value for $\tau_{9.7}$ measured for peak 1 might be caused by a dilution effect due to the large area covered by the IRS slit. If there is an extended component of mid-infrared continuum emission surrounding the SSC, this will be detected in the IRS slit, decreasing the depth of the silicate absorption features. This results in an underestimate of the extinction affecting the SSC.

Kunze et al. (1996) derived an extinction of $A_V \sim 70$ for the overlap region from ISO-SWS spectroscopy of the hydrogen recombination lines Brγ and Brα. This value, which is much higher than many other determinations for A_V, and the variations in

Table 5.8 — Extinction estimates

Position	A_V[a]	A_V[b]	A_V	$\tau_{9.7}^{e}$	$\tau_{9.7}^{f}$
peak 1	4.23	6.2 ± 0.3	4.3 ± 0.3[c]	≤ 0.86	0.19
peak 2	0.18	0.7 ± 0.1	1.4 ± 0.3[c]	≤ 0.69	0.13
longwave	11.81	10.3 ± 0.5	...	≤ 0.80	1.03
peak 3	0.14	4.8 ± 0.4	...	≤ 0.29	...
fuzz	...	...	0.72[d]	≤ 0.29	0.05
peak 4	...	...	0.6 ± 0.3[c]	≤ 0.18	...

[a] A_V from a comparison of near-infrared photometry of various broad- and narrow-band fluxes with *Starburst 99* (Mengel et al. 2005).

[b] A_V from Paβ and the Brackett series (Chapter 4).

[c] A_V from Brγ/Hα (Mengel et al. 2001).

[d] A_V from Hα/Hβ (Bastian et al. 2006).

[e] $\tau_{9.7}$ estimates from *PAHFIT*; all upper limits (Section 5.3.5).

[f] $\tau_{9.7}$ estimates from baseline fitting (Section 5.3.5).

the extinction values for individual sources in Table 5.8 show that there is generally very little agreement between any two different methods used to derive the extinction of SSCs in the Antennae.

We also note that optical methods mainly probe the absorption by graphite-based dust particles, while the mid-infrared methods are mainly sensitive to distinct silicate absorption. In the diffuse ISM graphite and silicate-based dust are uniformly mixed and tightly correlated (Roche & Aitken 1984). Recently, Chiar et al. (2007) found that in dense clouds with $A_V \geq 12$ the linear relation between optical and mid-infrared estimates breaks down and $\tau_{9.7}$ underestimates the real amount of dust. However, most of our regions are below $A_V \sim 12$ and the discrepancy between the extinction values in Table 5.8 is primarily given by systematic uncertainties rather than ISM chemistry.

5.4 Discussion

In this Section we will discuss and interpret our observational findings from both the spectral maps and the eight 'hires' spectra. Our aim is to characterize the conditions under which SSCs form and evolve, their properties, and how their presence affects the surrounding interstellar medium. We start with a discussion of the individual regions, discuss qualitatively the ISM properties across the central region of the Antennae, investigate dust temperatures and radiation field, and derive cluster star formation rates. We discuss the range of strengths of the PAH features and give special attention to the strength of the H_2 emission and the temperature and excitation of the molecular hydrogen in the Antennae.

5.4.1 The nuclei of NGC 4038 and NGC 4039

Given the early merger state of the Antennae system, the nuclei of NGC 4038 and NGC 4039 are still clearly separated and have been well studied individually. Based on sub-arcsecond near-infrared spectroscopy from Keck, Gilbert et al. (2000) found that the spectrum of the nucleus of NGC 4039 is characterized by a strong stellar continuum and bright, extended H_2 emission. These authors also found strong photospheric absorption of Mg I, Na I, and Ca I as well as from the CO $\Delta\nu = 2$ band head, indicating that the continuum is dominated by old giants and red supergiants. The Brγ line, an indicator of recent massive star formation, was not detected. Similarly, Mengel et al. (2001) found an age range of 65 ± 15 Myr from the CO absorption for both nuclei. In that paper starburst activity was identified a couple of arcseconds north of the K-band peak of the nucleus of NGC 4038, consistent with an age of around 6 Myr. However, it has been pointed out by Wang et al. (2004), based on IRAC observations that the two galactic nuclei have lower SFRs than the overlap region, despite the large nuclei.

The IRS observations of the two nuclei reveal two quite similar spectra (Fig. 5.2) in terms of their PAH strength and silicate absorption. However, the spectra differ in their mid-infrared flux and 20-30μm slope, and the fine-structure emission lines are significantly different. The ratio of [Ne III]/[Ne II] is 0.08 ± 0.02 in NGC 4038 and 0.47 ± 0.11 in NGC 4039, almost six times higher. Similarly, the [S IV] line is very strong in NGC 4039 while it has not been detected in NGC 4038. On the other hand, NGC 4038 has a flatter mid-infrared slope than NGC 4039, indicative of hotter dust in the lower excitation nucleus.

As mentioned in section 5.2.1, the observed position of the nucleus of NGC 4038 is slightly offset to the north of the radio nucleus, and the wide IRS-SH slit includes the nearby star forming region as well. Hence, the detected mid-infrared emission is most likely dominated by the starburst activity to the north of the nucleus of NGC 4038. The nucleus and the starburst can be seen in most of the spectral maps in Fig. 5.6 as an extended structure with two separate components. The contribution of the starburst would explain the relatively luminous and warm mid-infrared emission (cf peak 3 in Fig. 5.4), and its age of $\sim$6 Myr fits with the weak emission of the high-excitation fine-structure lines.

The strong high excitation lines in the NGC 4039 nucleus pose somewhat more of a problem. The cool mid-infrared emission argues against the presence of a strong heating source. However, the bright emission lines indicate that an energetic source must be present. The combination of cool continuum and high excitation lines may be produced by a weak active galactic nucleus in NGC 4039. In addition, the strong H_2 lines in this nucleus are a possible indication of shocks.

Chandra detected several X-ray sources near the radio position of the nuclei of NGC 4038 and NGC 4039 (Zezas et al. 2002a). The X-ray sources identified with the nuclei are both luminous and spatially extended. The NGC 4038 nucleus spectrum is very soft and steep, and consistent with thermal emission by a supernova-driven superwind, possibly with some contribution by X-ray binaries (Zezas et al. 2002a,b). The nucleus of NGC 4039 is more luminous in X-rays, but its spectrum also suggest a combination of X-ray binaries and compact supernova remnants (Zezas et al. 2002a,b).

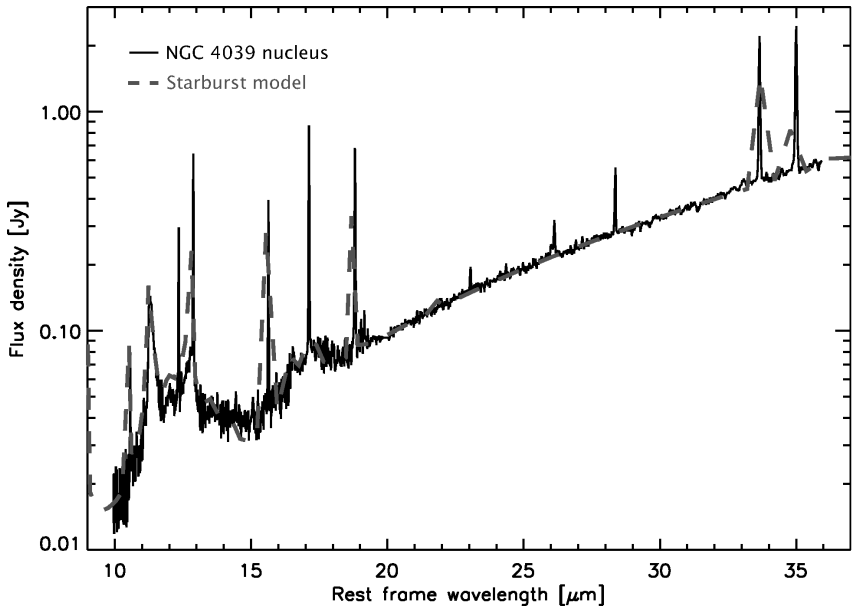

Figure 5.7 — IRS spectrum of the NGC 4039 nucleus (thin black curve) with the best fitting starburst SED model template from Groves et al. (2007) (thick dashed grey curve). The fit is constructed from a combination of several luminosity-weighted model SEDs in the age range of 0 - 10 Myr.

The NGC 4039 nucleus also has a very steep radio spectrum (Neff & Ulvestad 2000), suggesting that its radio emission is non-thermal, arising from supernova remnants. These observations are consistent with the intermediate starburst age of about 65 Myr estimated by Mengel et al. (2001). The supernovae may be responsible for heating the ISM in the nuclear region to the observed X-ray temperatures, and the X-ray emission and shocks arising from the supernovae may also be (partly) responsible for the high-excitation line emission.

Neither X-ray nor radio observations provide strong evidence for activity due to black hole accretion in either nucleus. In the mid-infrared, AGN activity can usually be traced by the [O IV] and [Ne V] emission lines (Weedman et al. 2005). However, the [Ne V] lines at 14.3 and 24.3μm were not detected in either nucleus, and the [O IV] line, which can be excited by various processes (Lutz et al. 1998), is equally weak in both nuclei (Tab. 5.5), providing no evidence for a hidden AGN. This result is consistent with the large equivalent widths of the PAH features (Tab. 5.4), which would not be expected in the surroundings of an accreting black hole (Weedman et al. 2005).

As a final test, in figure 5.7 we demonstrate that the mid-infrared continuum of NGC 4039 can arise purely from dust heated by star formation. In the figure, we overplot the IRS spectrum of NGC 4039 nucleus with a starburst SED model from Groves et al. (2007), with the close match indicating that no AGN contribution is necessary in the spectrum. The agreement between the mid-infrared continuum of the model spectrum of a relatively young stellar population ($\leq$ 10 Myr) and the observations, indicate that the mid-infrared continuum emission from this source can be explained by star formation only. This result indicates that, within the wide IRS slit, star formation does not necessarily result in a warm mid-infrared continuum.

5.4.2 The properties of individual SSCs

Apart from the nuclei our observations include six distinct regions of enhanced infrared luminosity. Their positions are illustrated in Fig. 5.1 and detailed in Tab. 5.2.

Four of these six clusters are located in the overlap region: peaks 1, 2, 3, and the long-wave peak; peak 4 and 'fuzz' are located outside the overlap region. In this section we summarize their individual properties, mainly based on information from the literature, which will be helpful for the subsequent discussion.

Peak 1

The mid-infrared observations with ISO have revealed that the so-called overlap region is the region of the most intense star formation in the Antennae (Mirabel et al. 1998; Vigroux et al. 1996). Peak 1 is the brightest infrared source in the overlap region. It coincides with a clump of molecular gas as traced by CO (peak CO_S and SGMC 4–5, Stanford et al. 1990; Wilson et al. 2000). The optical counterpart to this source is a very inconspicuous, faint, red source in the HST images (Whitmore & Schweizer 1995, source 80), obscured by large amounts of gas and dust. However, in the mid-infrared this single compact source with a radius smaller than 100 pc emits $\sim 15\%$ of the total 15μm luminosity of the Antennae.

Based on near-infrared spectral features, Mengel et al. (2001) derived an age of $5.5^{+0.7}_{-0.8}$ Myr. Using the instantaneous starburst models presented in Chapter 2 (Fig. 7 of that Chapter), the Brγ equivalent width (EW) in Mengel et al. (2005) suggests a lower limit of $2.3 - 4.0$ Myr. This is consistent with the age of ~ 4 Myr determined by Gilbert et al. (2000). However, several authors have argued that the stellar population is even younger. The analysis of near-infrared spectral lines (Chapter 4) leads to an age estimate of ≤ 2.5 Myr, which is in agreement with the age of about 2 Myr derived from the comparison of its optical colors with stellar population synthesis models (Whitmore & Zhang 2002). From the comparison of infrared spectra with *Starburst 99* models (Leitherer et al. 1999), the total stellar mass within the peak 1 region has been estimated to be $\sim 7 \cdot 10^6$ M$_\odot$ (Gilbert et al. 2000), $\sim 3.0^{+3.6}_{-0.7} \cdot 10^6$ M$_\odot$ (Mengel et al. 2001), and $1.1 - 1.2 \cdot 10^6$ M$_\odot$(Chapter 4).

The extinction toward peak 1 is considerable, with A_V estimates of 4.3 ± 0.3, 4.23, $9 - 10$, and 6.2 ± 0.3 (Mengel et al. 2001, 2005; Gilbert et al. 2000, and Chapter 4, respectively). These values are consistent with the lower limit of $A_V \geq 4$ derived from radio observations (Neff & Ulvestad 2000).

With fluxes of 4.7 mJy and 5.2 mJy at 4 cm and 6 cm, respectively, peak 1 is also the brightest source at centimeter wavelengths. The spectral index of the radio emission is relatively flat, indicating that the spectral energy distribution is dominated by the thermal radiation from H II regions, irradiated by the equivalent of ~ 5000 O5 stars. This is even more luminous than the equivalent of the 7000 O7 stars of the massive SSC estimated to be powering the center of NGC 5253 (Turner & Beck 2004). The total ionized gas mass derived from these radio data is $1.7 \cdot 10^6$M$_\odot$, with a lower limit on the electron density of $3.6 \cdot 10^2$ cm^{-3} (Neff & Ulvestad 2000). Based on sub-arcsecond near- and mid-infrared spectroscopic data, both Gilbert et al. (2000) and we (Chapter 2) and find a significantly higher ionized gas density of 10^4 cm^{-3}.

Peak 2

Peak 2 is the mid-infrared counterpart to a bright and blue complex of clusters, which contains eight optical sources within a region of 1."5, corresponding to 160 pc in pro-

jection (Whitmore & Schweizer 1995). This group of optical sources probably provides enough ionizing photons to account for the observed 4 and 6 cm radio emission. Peak 2 corresponds to the second brightest radio source in the Antennae with flux densities of 2.2 and 2.3 mJy at 4 and 6 cm, respectively. Like peak 1 it has a flat spectral slope typical for the emission from H II regions (Neff & Ulvestad 2000). The equivalent of $\sim$ 3000 O5 stars would be necessary to produce the measured fluxes, consistent with the lower limit of 300 O dwarfs derived from FUV observations (Neff et al. 1996).

Peak 2 is clearly less dust extincted than peak 1 (Tab. 5.8). The various age estimates range from zero to four million years and are listed in Table 5.9. Assuming a Salpeter (1955) IMF from $1 - 100$ $M_\odot$, Mengel et al. (2001) derived a total stellar mass of $1.6^{+1.2}_{-0.2} \cdot 10^6$ $M_\odot$, in agreement with the mass of $1.2 - 1.7 \cdot 10^6$ $M_\odot$found in Chapter 4 . The density of the ionized gas has been estimated to be $\sim 10^4$ cm^{-3} (Chapter 2).

Longwave

The brightest peak at sub-millimeter wavelengths (Klaas et al. 1997), 'longwave', is located in the overlap region approximately 2.3 kpc to the northwest of peak 1. It is one of the most heavily embedded clusters in the Antennae, with an A_V between 10 and 12 (Mengel et al. 2005, and Chaoter 4). Its optical counterpart is identified as the red source 115 in Whitmore & Schweizer (1995). The Brγ equivalent width suggests an age of 3 – 5 Myr (Chapter 4).

The 'longwave peak' coincides with the sources CO_W and SGMC 1 (Stanford et al. 1990; Wilson et al. 2000), which are huge concentrations of approximately $3.9 \cdot 10^8$ $M_\odot$ of molecular gas. At the same location is a very bright, compact radio source (Neff & Ulvestad 2000). The spectral slope of this source is rather steep, and the dominant emitters are most likely supernova remnants. The derived supernova rate is $9.8 \cdot 10^{-3}$ yr^{-1}, which supports the older age estimates for this source.

Peak 3

Peak 3 corresponds to the largest concentration of molecular gas in the overlap region. The coincident sources CO_F and SGMC 1 (Stanford et al. 1990; Wilson et al. 2000) contain a total molecular gas mass over $6 \cdot 10^8$ $M_\odot$. Peak 3 suffers intermediate extinction of $A_V \sim 4.8 \pm 0.4$ (Chapter 4). It is the brightest source in the near-infrared K-band (Brandl et al. 2005). The EW(Brγ), measured by Mengel et al. (2005), indicates an age of $3.2 - 4.9$ Myr, which is slightly older than the 2.0 Myr found by Whitmore & Zhang (2002), and the range of 1 – 3 Myr derived in Chapter 4.

The slope of the corresponding bright, compact radio source (Neff & Ulvestad 2000) is steep, arguing for a somewhat older cluster with its radio emission being dominated by supernova remnants. The derived supernova rate for this cluster is $4.8 \cdot 10^{-3}$ yr^{-1}.

Fuzz

The position labelled 'fuzz' is a mid-infrared source located in a region of more extended, "fuzzy" infrared emission, to the east of the nucleus of NGC 4038. From optical data, Bastian et al. (2006) determined a subsolar metallicity of $Z \sim 0.75 Z_\odot$ for this region. The various age diagnostics indicate that the stellar population is somewhat older here than in the overlap region, although the results have significant scatter. Whitmore & Zhang (2002) determined an age of 8.4 Myr from the optical colors,

while Mengel et al. (2005) derived an age of $4.3 - 5.7$ Myr from the equivalent width of the Brγ line, and Bastian et al. (2006) argue for $3.0 - 4.5$ Myr, based on the presence of strong Wolf-Rayet emission features in the optical spectra. Mengel et al. (2005) conclude that the cluster at position 'fuzz' does not suffer from extinction. However, Bastian et al. (2006) derive an $A_V \sim 0.72$ from their optical spectra.

The spectral slope of the radio fluxes in this region is right at the division point between H II regions and supernova remnants as the source of radio emission. The inferred supernova rate for the latter is lower than for the other sources at $0.3 \cdot 10^{-3}$ yr^{-1} (Neff & Ulvestad 2000).

Peak 4

Finally, peak 4 is located to the far west of the nucleus of NGC 4038. The independent age determinations by Mengel et al. (2002) and Whitmore & Zhang (2002) agree that this cluster is around $6.6 - 7$ Myr old. The radio observations show a moderately bright, compact source with a steep spectral slope, indicative of an evolved stellar population. The supernova rate is calculated to be $1.0 \cdot 10^{-3}$ yr^{-1} (Neff & Ulvestad 2000).

5.4.3 Cluster ages in comparison

The age estimates depend significantly on the method being used, and show significant scatter. The literature values on cluster ages and stellar cluster masses for all our clusters are summarized in Table 5.9. Generally, the various age diagnostics indicate that the luminous infrared sources in the northern part of the overlap region are somewhat older than the ones in the more active, southern overlap region.

Table 5.9 — Cluster Ages from the Literature

Position	Age[a] (Myr)	Age[b] (Myr)	Age[c] (Myr)	Age[d] (Myr)	Age[e] (Myr)
peak 1	2.0	$2.3 - 4.0$	3.5	≤ 2.5	2.5
peak 2	3.8	$2.3 - 4.0$	...	≤ 3	3.0
longwave	...	$3.7 - 5.1$	5.7	$3 - 5$	4.5
peak 3	2.0	$3.2 - 4.9$	3.9	≤ 3	3.0
fuzz	8.4	$4.3 - 5.7$	...	...	6.0
peak 4	7.0	≥ 6	...	...	7.0

[a] From Hα (Whitmore & Zhang 2002)
[b] From Brγ equivalent width (Mengel et al. 2005)
[c] From Brγ equivalent width (Gilbert & Graham 2007)
[d] From the equivalent width of several hydrogen Recombination lines (Chapters 2 and 4)
[e] Average age from the listed estimates

In Fig. 5.8 we compare the averaged values for the cluster ages from the literature to the radiation hardness measured by the [Ne III]/[Ne II] line ratio. Within the systematic uncertainties there is a very good correlation showing that older clusters have a softer radiation field. The scatter in the age range of 2.5 – 5 Myr is not surprising, given that a small number of Wolf-Rayet stars at that age will significantly harden the observed radiation field. It is reassuring that completely independent methods lead to consistent results.

We note that starburst activity exists to both east (including 'fuzz') and west (in-

cluding peak 4) of the nucleus of NGC 4038 at almost the same level, in terms of the [Ne II] and PAH intensity. Interestingly, peak 4 and 'fuzz' have almost identical mid-infrared spectra (Fig. 5.4), yet are separated by more than 2.4 kpc in projection. With a velocity dispersion of ~ 10 km s^{-1}, (Whitmore et al. 2005) the dynamical time to connect the two points would be 235 Myr, more than an order of magnitude longer than the cluster ages. This suggests that the dominant mode of starburst triggering is not propagating globally across the system but is governed by processes on smaller scales.

5.4.4 The physical conditions across the Antennae

In this subsection we discuss the spatial variations in the ISM as revealed by the spectral maps shown in Fig. 5.6. These maps provide a more global picture of the physical conditions across the central region of the Antennae galaxies. Unfortunately, the [Ne III] line, which we will utilize heavily in Section 5.4.5, is not covered by the IRS-SL module. It is observed with the IRS-LL module, but this has a significantly wider slit. However, given that the excitation potential of [Ne III] (40.96 eV) is reasonably close to that of [S IV] (34.8 eV), we substitute the [S IV] line as a tracer of the harder radiation.

Fig. 5.6 (top) compares the maps of [Ne II] with [S IV]. It takes only 21.6 eV to excite [Ne II], and the emission traces primarily the regions where star formation occurred in the past ~ 10 Myr (as a rule of thumb we assume that [Ne II] is primarily sensitive to stars younger than ~ 10 Myr, while [S IV] traces stars younger than ~ 6 Myr in a starburst). The [Ne II] emission also follows roughly the structure of the Hα maps by HST (Whitmore et al. 1999). The [S IV] emission originates predominantly from the two clusters, peak 1 and 2 in the overlap region, with peak 2 being even brighter in [S IV] than peak 1 (Fig. 5.6). Although this has already been indicated by the spectra in Figs. 5.3 and 5.4, and qualitatively known since ISO (Mirabel et al. 1998) it is once again remarkable how the bulk of the current massive star formation in such an interacting system, which extends over many kiloparsecs, is confined to just two compact regions. Some [S IV] emission is also detected from the nucleus of NGC 4039, but none from 4038 (Section 5.4.1). The [Ne II] map is dominated by the two clusters peak 1 and 2 as well, although to a much lesser degree than the [S IV] map, and also shows emission from the nucleus of NGC 4038. Noticeable [Ne II] emission is also detected to the west of the nucleus of NGC 4038, where numerous older SSCs reside (Mengel et al. 2005).

Overall, the PAH maps in Fig. 5.6 (center row) resemble the [Ne II] map[2], but show noticeably more diffuse emission (this is not just a signal-to-noise effect). The PAH maps trace the PDRs and hence in general the environment of OB clusters. However, the fact that the [Ne II] and PAH map resemble each other qualitatively implies that we do not resolve the H II region/PDR interfaces at the spatial resolution of the IRS-SL spectral map, which is around 360 pc. The most obvious difference between the [Ne II] and the PAH maps is the strength of peaks 1 and 2 relative to the nucleus of NGC 4038. The latter is the dominant source of PAH emission, while the embedded SSCs play only a minor role. Within the uncertainties, which are dominated by the lower signal-to-noise in the 6.2μm map, we find no significant differences between the

[2]See section 5.3.3 for a discussion of the possible contamination of [Ne II] by the 12.7μm PAH emission in 'lores' mode.

11.3μm and the 6.2μm PAH maps (note that the PSF in the former is also 1.8 times larger). The similarity between the two PAH maps agrees with our study of the PAH spectrum in Section 5.4.7.

The bottom row in Fig. 5.6 shows the spectral maps in the H_2 S(2) and S(3) lines. Both maps are very similar. We find that approximately 45% of the total H_2 S(3) emission comes from a slightly extended region around southern nucleus, NGC 4039. The nucleus of NGC 4038 does show some H_2 emission, but very little compared to NGC 4039. The emission peaks of the clusters in the overlap region are more compact and also weaker. Most interesting here is the spatial offset of about 3.″5 , which approximately corresponds to 370 pc in projection, that exists between the peaks of H_2 emission and the spectral continuum, for both, the 'longwave' peak and the nucleus of NGC 4039. The H_2 S(2) emission peaks to the south in both objects and appears also, at least near the nucleus on NGC 4039, more extended. Since the offsets are with respect to the continuum emission, which was simultaneously observed with the line emission, they cannot be due to spacecraft pointing errors or other observational ef-

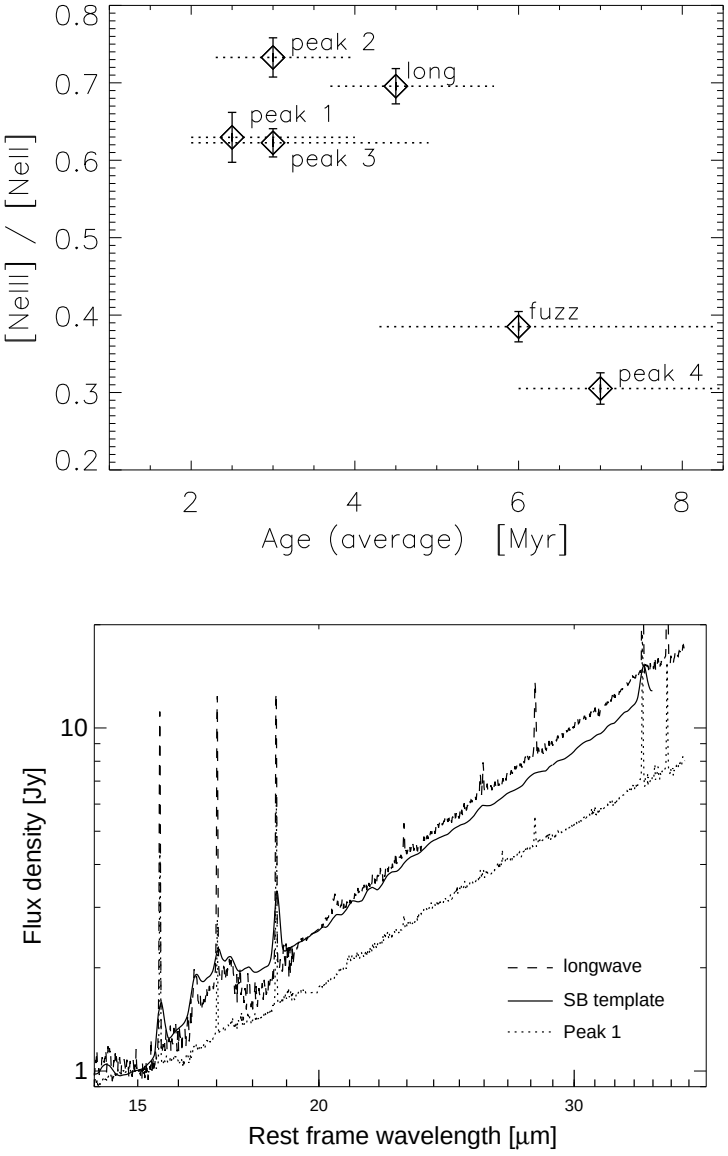

Figure 5.8 — *Top:* The hardness of the radiation field (as measured by the line flux ratio of [Ne III]/[Ne II]) versus the average age of the SSCs from Table 5.9. The horizontal dotted lines indicate the age ranges covered by the various estimates. *Bottom:* Comparison of the $14 - 37\mu$m continuum slopes for three selected objects: peak 1 and longwave with the most shallow and steep slopes in our sample of Antennae clusters, and the average starburst template spectrum from Brandl et al. (2006). All spectra have been normalized to a flux density of unity at 15μm.

fects. Rather they may arise from a physical displacement between the massive SSCs and the source of H_2 emission.

We note that there is an obvious lack of correspondence between the H_2 and the PAH maps, although both species are generally thought to originate from the same PDR regions if the H_2 is UV-excited. This discrepancy is also (and independently) shown in Fig. 5.11. Similar results based on observations of the starburst nucleus of M83 will be reported in Chapter 6. A possible explanation for the morphological differences is the effect of varying ISM densities, which is known to have a considerable impact on the line intensities of the mid-infrared rotational H_2 lines (Fig. 3 in Burton et al. 1992).

We also compared our 8.6μm PAH map with the IRAC 8μm image of Wang et al. (2004). Overall, despite the slightly better spatial resolution of the IRAC image both maps look very similar with one exception: the emission from peak 1 is noticeably brighter in the IRAC image than in the 8.6μm PAH map. The spectra in Figs. 5.3 and 5.4 and the values in Table 5.4 show that the PAH equivalent widths of peaks 1 and 2 are significantly below those of the other clusters. Although the IRAC 8μm band is generally dominated by PAH emission, a proper continuum subtraction is obviously important for more quantitative estimates.

5.4.5 Dust temperature and radiation field

The mid-infrared continuum longward of $\sim 20\mu$m is produced by the thermal emission from dust heated by the stellar clusters. The slope of the continuum represents the temperature distribution of the dust. The presence of a hot dust component (100 K $\leq T \leq$ 250 K) flattens the continuum slope in the wavelength range of $15 - 35\mu$m, while a cold dust component ($T \leq 50$ K) steepens the slope. The continuum fluxes at 15μm and 30μm and their ratio are listed in Table 5.3. Peaks 1 and 2 have the shallowest slopes, indicating the highest dust temperatures, while peak 3 and 'longwave' show the steepest continua, evidence for a dominating dust component at lower temperature. The difference is also illustrated in Fig. 5.8 (bottom panel) for the most extreme cases peak 1 and 'longwave', in comparison to the average starburst galaxy spectrum from Brandl et al. (2006). The slope of the starburst template lies between the two Antennae clusters, suggesting that the dust temperatures in starburst environments are determined on small scales.

Generally, the dust temperature depends on a complex relation between ISM density, grain size distribution, stellar properties, strength of the radiation field, and the local geometry of cluster, H II region, PDR, and surrounding ISM. We have investigated possible correlations of the dust temperature with cluster properties from the literature and our measurements, such as cluster age (Table 5.9), near-, mid-infrared or radio luminosities (Tables 5.9,5.3), extinction (Table 5.8), PAH strength (Table 5.4) or star formation rates. No convincing correlation between those parameters was found.

5.4.6 Star formation rates for the individual star-forming regions

The mid-infrared continuum fluxes can also be used to estimate the total infrared luminosity of starburst systems (in which $L_{IR} \approx L_{bol}$). In their Section 4.2, Brandl et al.

(2006) discuss a method based on the 15μm and 30μm continuum fluxes. Adopting their empirical relation and a distance of 21 Mpc (Stanford et al. 1990), we get $L_{IR} = 1.883 \cdot F_{15} + 4.851 \cdot F_{30}$ in units of $10^9 L_\odot$. We note that this empirical relation was derived for global starbursts, where the temperature components may differ from those in and around more compact SSCs. However, the good agreement in Fig. 5.8 between the slopes of the various systems suggests that the estimate works reasonably well.

In Table 5.10 we list the mid-infrared derived cluster luminosities. The infrared luminosities of the eight compact regions listed in Table 5.10 already add up to $L_{IR} = 3.5 \cdot 10^{10} L_\odot$. For a distance of 21 Mpc the total infrared luminosity of the Antennae as measured by ISO is $L_{IR} = 6.4 \cdot 10^{10} L_\odot$(Klaas et al. 1997). The eight sources studied in the Chapter together are responsible for more than half of the infrared luminosity of the entire system.

Kennicutt (1998) has shown that the $8 - 1000\mu$m infrared luminosity L_{IR} of starbursts is a good measure of the SFR as given by

$$\mathrm{SFR}\ [M_\odot \mathrm{yr}^{-1}] = 4.5 \cdot 10^{-44} L_{IR}\ [\mathrm{erg\ s}^{-1}]. \tag{5.7}$$

We note that the SFR conversion given by Kennicutt (1998) strictly applies only to dusty starbursts in the continuous star formation approximation, with ages of order $10 - 100$ Myr. Our clusters are significantly younger than that, so in the continuous star formation approximation (which is a reasonable one, given the more or less continuous range of cluster ages, Fig. 5.8) the IR luminosity per unit mass of stars formed will be somewhat lower. In other words, our estimate will systematically underestimate the SFRs.

Using relation from Kennicutt (1998), we estimate significant star formation activities for the individual clusters (Table 5.10). This disagrees with Schulz et al. (2007), who found no signs of intense starburst activity associated with their GMCs. If we co-add the eight regions we get SFR $\approx 6 M_\odot$ yr^{-1}, which is a lower limit, since we included only the most luminous clusters. Hence, the total SFR for the Antennae may be a factor of two higher, which would bring it close to the SFR of $23.8 M_\odot$ yr^{-1} derived by Zhang, Fall & Whitmore (2001), corrected for our adopted distance to the Antennae.

5.4.7 PAHs – Strengths and variations

PAHs are considered the most efficient species for stochastic, photoelectric heating by UV photons in PDRs (Bakes & Tielens 1994). They are usually a good tracer of starburst activity in a statistical sense (e.g., Brandl et al. 2006, and references therein). However, numerous studies over the past two decades (e.g. Geballe et al. 1989; Cesarsky et al. 1996; Tran 1998) have shown that intense UV fields can lead to the gradual destruction of PAH molecules. A clear anti-correlation between the 11.3μm PAH strength and the radiation field across the central region of NGC 5253 was recently observed by Beirão et al. (2006). We investigate a similar scenario in the Antennae in two different ways: via a pixel-by-pixel analysis within the spectral map and for the eight 'hires' spectra. The former is shown in Fig. 5.9 where the 11.3μm PAH-to-continuum ratio is plotted versus the hardness of the radiation field as expressed by the line ratio of [S IV]/[Ne II]. Each

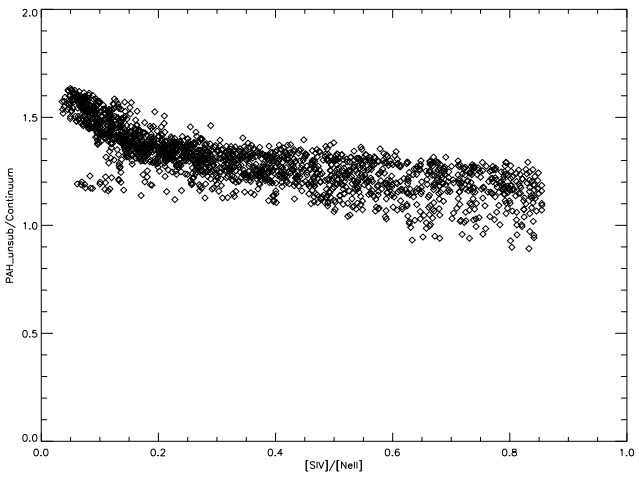

Figure 5.9 — The relative strength of the 11.3μm PAH feature ("line"-to-continuum ratio) versus the hardness of the radiation field as expressed by the line ratio of [S IV]/[Ne II]. Each data point corresponds to a pixel in our spectral map.

data point in Fig. 5.9 corresponds to a spatial pixel in our spectral map[3]. Because of the low signal-to-noise in the [S IV] line map, many data points represent a 3σ upper limit on the [S IV] measurements. Without upper limits the points would be more stretched toward the left, qualitatively not affecting the observed anti-correlation.

However, the strength of the [S IV] relative to the [Ne II] line does not only depend on the hardness of the radiation field, but is sensitive to the gas density as well. Given the critical densities of $3.7 \cdot 10^4$ cm^{-3} and $6.1 \cdot 10^5$ cm^{-3} for [S IV] and [Ne II], respectively (Tielens 2005), it is expected that ISM densities above 10^4 cm^{-3} will cause a lower [S IV]/[Ne II] ratio. The "outliers" in the second, lower branch around [S IV]/[Ne II] ~ 0.1 belong to peaks 1 and 2. It is not likely that the low [S IV]/[Ne II] line ratio values, measured for the two most active star-forming regions, are a result of a relatively soft radiation field. This hypothesis is also supported by the relatively high [Ne III]/[Ne II] ratio measured for these two sources (Fig. 5.8). Model calculations with *Mappings* show that an increase in density from 10^4 to 10^5 cm^{-3} causes [S IV]/[Ne II] to decrease by a factor of three. Hence, the low observed value of [S IV]/[Ne II] probably indicates that peaks 1 and 2 reside in a high density ISM, and the different critical densities shift the data points to the left, creating the second, lower branch in the diagram. Overall, we observe a trend of reduced PAH strength at locations with harder radiation field.

To quantify the strength of the radiation field we use the following parametrization, following Beirão et al. (2006).

$$([\mathrm{Ne\,II}] + [\mathrm{Ne\,III}]) \times \frac{[\mathrm{Ne\,III}]}{[\mathrm{Ne\,II}]}. \tag{5.8}$$

The first term, ([Ne II] + [Ne III]), is a measure of the intensity of the field, assuming that all Neon exists in one of the two ionization states. The second term, [Ne III]/[Ne II], is a measure of the radiation field hardness. We define the product of intensity and hardness as the strength of the radiation field. In Fig. 5.10 we plot the strength of the

[3]See section 5.3.3 for a discussion of the possible contamination of [Ne II] by the 12.7μm PAH emission in 'lores' mode.

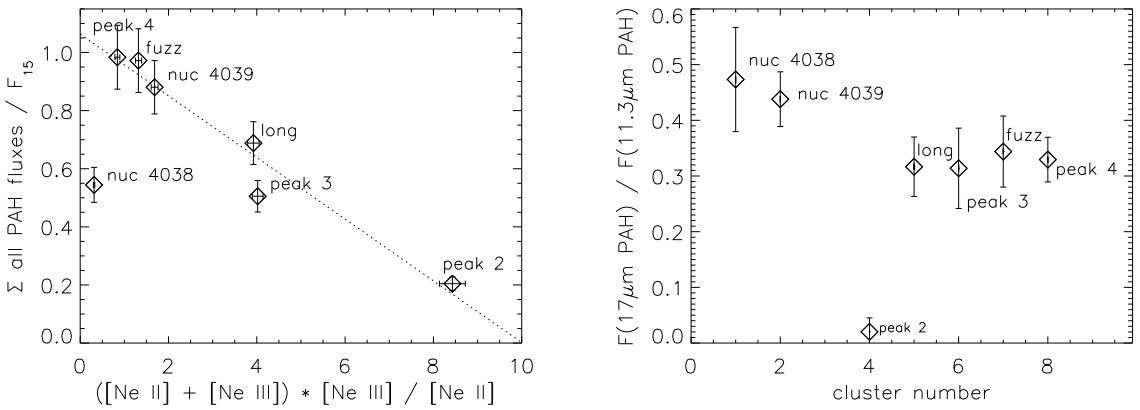

Figure 5.10 — *Left:* The relative strength of all PAH features within the $10 - 20\mu$m range versus the strength of the radiation field (in 10^{-13} erg sec^{-1} cm^{-2}). *Right:* The flux ratio of the PAH complex at 17μm (sum of the features at 16.5μm, 17.4μm and 17.9μm) to 11.3μm. The units on the x-axis are consecutive position numbers. In both panels peak 1 is not included in this table since *PAHFIT* did not yield reliable fit results (see main text for discussion).

PAH features, measured from the 'hires' spectra, against the strength of the radiation field as defined in Section 5.4.5. On the ordinate we plot the average PAH strength calculated by co-adding all the PAH fluxes listed in Table 5.4 and normalizing them to the 15μm continuum flux (Table 5.3). There is a clear linear anti-correlation between the strengths of the PAH emission and the radiation field. The only outlier is the nucleus of NGC 4038, which is less actively forming stars than the other sources.

Both rather independent methods and data sets provide strong statistical evidence that the strength and hardness of the radiation field affect the observed PAH emission. However, we cannot be certain that this effect is actually due to a destruction of PAH molecules in stronger radiation fields. The regions with the strongest PAH "equivalent width" are peak 4 and 'fuzz'. Both are located in less dense regions of the Antennae. These clusters are also slightly older and have had more time to shape the surrounding ISM via stellar winds and SNe. If the size of the emitting region is radiation-bounded these regions may just have "grown" more complex H II region/PDR interfaces from where the PAH emission originates. In other words, the PDR surface area is higher relative to the thermal emission from dust in the denser regions, which produces the underlying continuum.

We cannot resolve the H II region/PDR interfaces with the IRS-SH with a slit width corresponding to 360 pc. However, some of the clusters were recently observed by Snijders et al. (2006) with VISIR on ESO's VLT with a sub-arcsecond slit corresponding to only 50 pc (Chapter 3). Comparing the IRS-SH spectra of peaks 1 and 2 presented here to the VLT-VISIR spectra, we found in Chapter 3 that, while the continuum fluxes observed with both instruments are similar, the wider IRS slit detects significantly more PAH emission. It was concluded that a large fraction of the PAH emission cannot be directly associated with the SSCs but originates from an extended region around the cluster. The individual clusters are by far the most luminous sources on projected scales of a few hundred parsecs, and we may observe the profound effect of the OB

clusters on their surrounding ISM. However, if the space density of young clusters near peaks 1 and 2 is significantly higher than elsewhere it could also be that the PAH "excess emission", picked up only by the IRS, is unrelated to the main clusters and externally excited by smaller clusters in the surrounding field. At this point we cannot distinguish between the two scenarios.

Now we will investigate relative variations of the PAH spectrum. The PAH spectrum is expected to depend on the size of the PAH molecules. Smaller PAHs are more likely to emit at shorter wavelengths while larger PAHs are more likely to produce stronger features at longer wavelengths (Draine & Li 2001, 2007). Here we use the IRS 'hires' spectra to compare the 11.3μm feature to the 17μm PAH complex. The latter was first reported in extragalactic sources by Sturm et al. (2000) and is probably due to C–C–C bending modes (van Kerckhoven et al. 2000). Fig. 5.10 shows the ratio of the two features. For most sources the ratio is around 0.4, showing very little variations in the PAH spectrum features that are well separated in wavelength. The only exception is peak 2, which has no detection of the 17.4μm feature.

Another cause of potential variations of the PAH spectrum could be ionization effects. Several authors (e.g., Verstraete et al. 1996; Vermeij et al. 2002; Förster Schreiber et al. 2003) have found variations in the PAH spectrum, and that the C–C stretching modes at 6.2μm and 7.7μm are stronger in ionized PAHs, relative to the bending modes at 8.6μm and 11.3μm, by a factor of up to two. A comparison between the PAH maps in Fig. 5.6 does not reveal any significant differences apart from the spatial resolution. We also compare the spectral maps of the 11.3μm C–H out-of-plane bending mode to the 8.6μm C–H in-plane bending mode (Figure not shown in this Chapter). We have chosen these two for a direct comparison because of their proximity in wavelength (same beam size), similar susceptibility to dust extinction, and because both are observed through the same IRS (sub-)slit. Hudgins & Allamandola (1995) and Joblin et al. (1996) have argued that this ratio is also sensitive to the charge state of the PAH molecule. However, both maps trace each other extremely well with no significant differences on the scales that can be resolved with the IRS. In summary, we do not find any systematic variations of the PAH spectrum – except for peaks 1 and 2 where the 17μm complex is much weaker – that could be correlated with physical properties.

5.4.8 The strength of the H_2 emission

Molecular hydrogen is the most abundant molecule in the Universe. It plays a central role in star formation, not only as the major ingredient to build up a star but also as the coolant to permit an isothermal collapse of the gas cloud. The density and temperature of the H_2 molecule are of utmost importance for the processes in starbursts. However, the H_2 molecule is symmetric, has no dipole moment, and the mid-infrared lines originate from quadrupole rotational transitions. Consequently, the lines are intrinsically weak and usually hard to detect. Nevertheless, the H_2 lines in the spectra of the Antennae are amongst the strongest detected lines (Figs. 5.2, 5.3, and 5.4).

Since the first study of the S(2) line in Orion by Beck et al. (1979), and the detection of the S(0) line in NGC 6946 by Valentijn et al. (1996), the mid-infrared rotational lines in starbursts have been studied by numerous groups. The most relevant ones here are the ISO-SWS study of starburst and Seyfert galaxies by Rigopoulou et al. (2002),

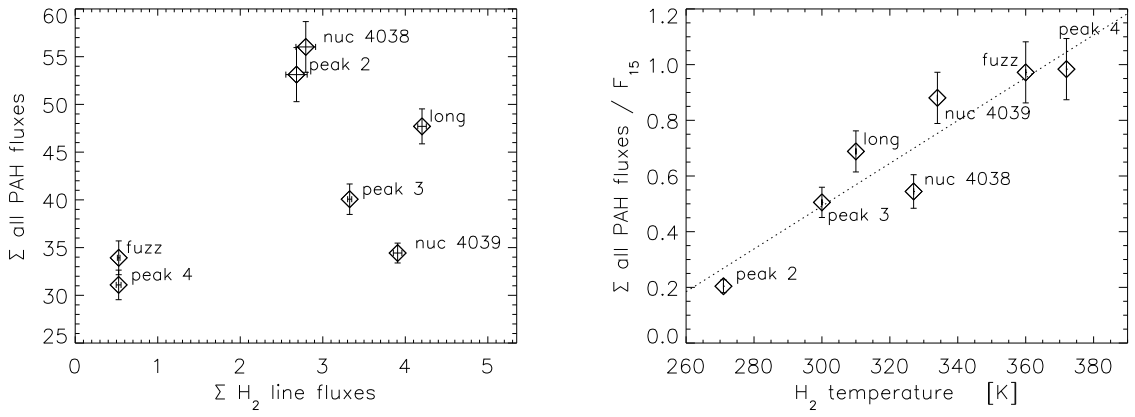

Figure 5.11 — *Left:* The flux from all tabulated PAH emission features between $10-20\mu$m versus the sum of the three rotational H_2 emission lines S(0), S(1), and S(2) (both in 10^{-13} erg sec^{-1} cm^{-2}). *Right:* The relative strength of the PAH emission (given by the flux sum of all PAH features between $10-20\mu$m normalized to the continuum flux at 15μm) versus the temperature of the H_2 gas from the S(2) and S(1) lines (Table 5.7). Peak 1 is again nog included, since *PAHFIT* did not yield reliable fit results (see main text for discussion).

who found warm H_2 at $T \sim 150$ K which accounts for about 10% of the total mass. A review of the extensive ISO studies of molecular hydrogen is given by Habart et al. (2005). Spitzer-IRS studies have been performed on large samples of ULIRGs (Higdon et al. 2006), starbursts (Devost et al. 2007), and the SINGS galaxy sample (Roussel et al. 2007). Here we investigate with which other observables the strong H_2 emission might be correlated.

Rigopoulou et al. (2002) found a good correlation between the 7.7μm PAH emission and the H_2 S(1) line luminosity in ULIRGs, within the spatially integrating ISO-SWS beam. A tight correlation between the H_2 line fluxes and the PAH fluxes was also reported by Roussel et al. (2007) for the SINGS galaxies (their Figs. 8c and 9). They explain it by the fact that both H_2 and PAHs are tracers of PDRs and therefore related. However, while PAH emission is almost exclusively excited by UV photons, H_2 can be purely UV pumped or collisionally excited (Section 5.3.4 and the extensive discussion in Chapter 4). The latter becomes important above the critical density of typically $\sim 10^3\,\mathrm{cm}^{-3}$, which is exceeded in our embedded SSCs, where densities of $1-4\cdot10^4\,\mathrm{cm}^{-3}$ (Schulz et al. 2007, and Chapter 2) or even higher (Mirabel et al. 1998) have been measured. The lack of spatial correspondence between the PAH emission and the H_2 emission in Fig. 5.6 is remarkable, and indicates that thermal excitation of the H_2 emission is probably dominant. Fig. 5.11 shows the total flux from the PAH features between $10-20\mu$m plotted against the sum of the fluxes of the three rotational H_2 emission lines S(0), S(1), and S(2). There is no apparent correlation between the PAH and H_2 line fluxes for the eight observed Antennae sources. It is also noteworthy that the two nuclei with the older stellar populations do not separate from the SSCs in this plot but lie within the same parameter space. We note that Roussel et al. (2007) based their PAH index on the 7.7μm micron feature, whereas our PAH index is based on the emission longward of 10μm. However,

since we do not observe any significant variations of the PAH spectrum (section 5.4.7 and Fig. 5.6) we assume that both measures are equivalent.

In Fig. 5.11 we show a correlation between the *relative* strength of the PAH emission features (as given by the flux sum of all PAHs between $10 - 20\mu$m normalized to the continuum flux at 15μm) and the temperature of the H_2 gas (as calculated from the S(2) and S(1) line). There is a clear tendency that the PDRs that are more efficient PAH emitters (relative to the continuum emission) have, on average, warmer molecular gas.

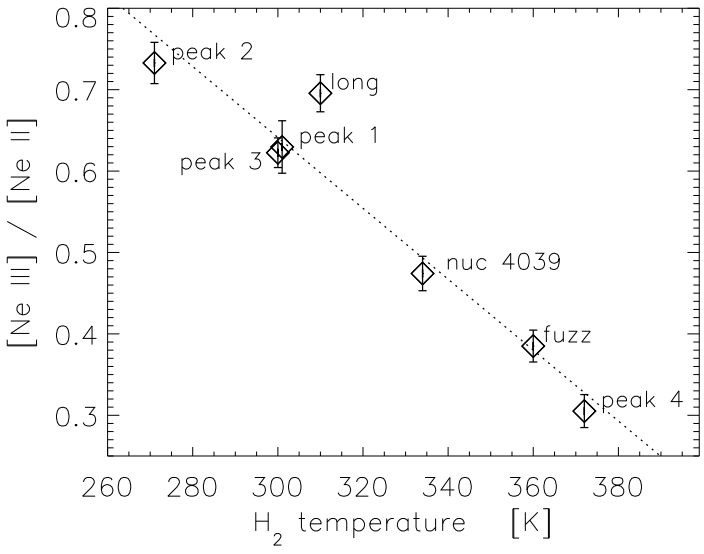

Figure 5.12 — The hardness of the radiation field (as given by the line flux ratio of [Ne III]/[Ne II]) versus the temperature of the H_2 gas from the S(2) and S(1) lines (Table 5.7). One outlier, the nucleus of NGC 4038 which shows a very low [Ne III]/[Ne II] ratio, is not included.

In Fig. 5.12 we plot the hardness of the radiation field in terms of [Ne III]/[Ne II] versus the temperature of the H_2 gas as calculated from the S(2) and S(1) line. There is an almost perfect anti-correlation between hardness and temperature. Warmer PDRs are clearly associated with a softer radiation field. This finding may, at first, be surprising as one might have naively guessed that a harder radiation field is more energetic and will lead to warmer dust. However, that does not apply to stochastically heated dust grains. Here a geometrical argument, similar to the scenario discussed in Section 5.4.7 may apply: The older, more evolved clusters had more time to shape the surrounding ISM via stellar winds and SNe, and the surrounding, clumpy dust and gas clouds have evolved into larger entities. The UV photons from the cluster can penetrate farther into the cloud and provide a more uniform temperature distribution over a larger area. Very young clusters may have hotter dust near their inner shell but are colder at their well shielded outskirts.

5.4.9 H_2 temperatures and masses

From a sample of 77 ultra-luminous infrared galaxies (ULIRGs) observed with the IRS, Higdon et al. (2006) measured a mean temperature of the warm H_2 gas of 336 K. For the more quiescent galaxies in the SINGS sample, Roussel et al. (2007) determined a median temperature of only 154 K. However, the slit apertures of the SINGS observations sample the circumnuclear regions, and often the spectra have contributions from multiple emitting sources, and presumably regions with a range of densities and tem-

Table 5.10 — Derived Cluster Properties

Position	L_{IR}[a,f] ($10^9 L_\odot$)	SFR[f] ($M_\odot$/yr)	T(H_2)[b] (K)	T(H_2)[c] (K)	M(H_2)[d] ($10^6 M_\odot$)	M(H_2)[e] ($10^6 M_\odot$)
nuc 4038	3.32	0.58	337	327	2.0	2.8
nuc 4039	1.68	0.30	370	334	5.7	4.4
peak 1	10.32	1.82	< 500	301	...	4.0
peak 2	9.41	1.66	299	271	3.2	3.8
longwave	3.50	0.62	289	310	5.5	5.2
peak 3	3.94	0.69	309	300	2.5	4.2
fuzz	1.19	0.21	...	360	...	0.4
peak 4	1.17	0.21	...	372	...	0.3

NOTE. – For uncertainties in the H_2 mass and temperature estimates see Section 5.3.4. Since the S(3) measurement of peak 1 is affected by a data artifact we give only an upper limit for the T(H_2).

[a] Luminosity estimate following Brandl et al. (2006)

[b] From the 'lores' S(3) and S(2) line fluxes

[c] From the 'hires' S(2) and S(1) line fluxes

[d] From the 'lores' S(2) line flux and temperature

[e] From the 'hires' S(2) line flux and temperature

[f] These values depend on the applied distance, which is 21 Mpc. In case of the lower distance of13.8 Mpc (Saviane et al. 2004), the values will decrease by a factor of 2.3.

peratures. For the Antennae galaxies Kunze et al. (1996) derived an H_2 temperature of 405 K from ISO-SWS data, whereas Fischer et al. (1996) used ISO-LWS and derived a temperature for the PDR of 200 ± 60 K. These temperatures are derived by different methods, Kunze et al. (1996) derive a temperature from the ratio between the 0-0 S(2) and the 0-0 S(1) H_2 lines, and Fischer et al. (1996) derive average properties of the PDR based on several carbon, oxygen, and nitrogen fine-structure lines between 50 – 160 μm. Furthermore, in Fischer et al. (1996) the line strengths are measured in an aperture that is $\sim$2.4 times larger than that of Kunze et al. (1996), which can explain a lower average gas temperature as well.

Our temperature and mass estimates for the different regions are listed in Table 5.10. The methods we used to calculate them are described in Section 5.3.4 together with a discussion of the systematic uncertainties. We can "simulate" a larger slit aperture (e.g., of ISO-SWS) by calculating the luminosity-weighted mean temperature for the clusters within the overlap region from the S(2) and S(1) lines. This yields a temperature of 295 K, which lies between the temperature estimates of Kunze et al. (1996) and Fischer et al. (1996).

To derive the fraction of warm H_2 to the total molecular gas we compare our measurements to the CO observations of Wilson et al. (2000) and Gao et al. (2001). Recently, Schulz et al. (2007) reported that the gas properties in the Antennae do not deviate significantly from the N_{H_2}/I_{CO} ratio found for the disk of the Milky Way, and

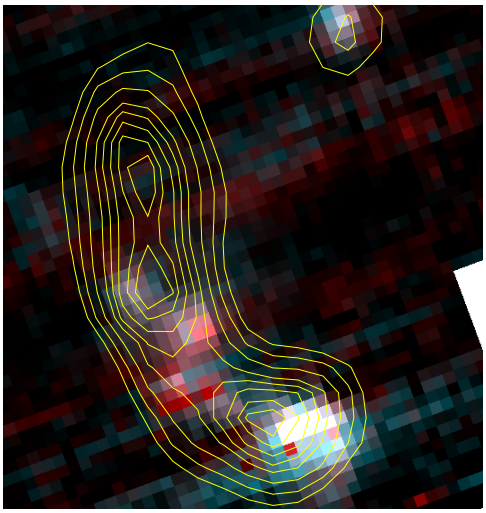

Figure 5.13 — IRS spectral map of a combination of the H_2 S(3) and the S(2) line. Brighter colors mean warmer H_2. The hottest emission originates from the nucleus of NGC 4039, the brightest source in this Figure. The emission from the overlap region and the nucleus of NGC 4038 is considerably cooler, which corresponds to lower temperature gas and fainter sources in this image. The two nuclei and the emission from the clusters in the overlap region are clearly visible. The white contour lines indicate the ISOCAM-CVF measurements of the H_2 S(3) line by Haas et al. (2005); the levels are at 39%, 49%, 58%, 68%, 78%, 84%, 90%, and 96% of the maximum intensity (see Fig. 2 in Haas et al. (2005)).

the conversion from CO is thus reasonably accurate. Wilson et al. (2000) used a CO to H_2 conversion factor of $3 \cdot 10^{20}$ $H_2\,cm^{-2}$, and derived a total H_2 mass of $5.3 \cdot 10^9 M_\odot$ for a distance of 19 Mpc.Gao et al. (2001) yielded a total H_2 mass of $1.5 \cdot 10^10 M_\odot$ ($D = 21$ Mpc). Adding up our estimates of warm molecular gas masses (Table 5.10) yields $M_{H_2}^{warm} = 2.5 \cdot 10^7 M_\odot$, and the resulting fraction of warm-to-total molecular gas mass is $3-5$ promille. This value is only a lower limit. The fraction has to be compared to typical values of $1-10\%$ in starburst galaxies and non-AGN dominated ULIRGs (Rigopoulou et al. 2002). While this fraction tends to be even higher in AGN dominated systems (up to 35% Rigopoulou et al. 2002) the Antennae appears to have, for its luminosity, an relatively low fraction of warm-to-total molecular gas mass.

Fig. 5.13 shows a combined image of the IRS maps with the H_2 S(3) and S(2) lines (cp. to Fig. 5.6). Both nuclei and the emission from the active overlap region are clearly visible. From the spectral map we measure a total integrated H_2 S(3) flux of $1.0 \cdot 10^{-12}$ erg sec^{-1} cm^{-2}. This is a factor 3.3 times lower than the corresponding line flux measured by Haas et al. (2005). At a distance of 21 Mpc the S(3) line flux corresponds to a line luminosity of $1.4 \cdot 10^7 L_\odot$. Using the far-infrared luminosity derived by Klaas et al. (1997) we calculate the ratio to be $L(H_2)/L_{IR} \approx 1.2 \cdot 10^{-4}$. This value is only slightly larger than the one for M82, and is not unusual for starbursts and ULIRGs in general (cf. Haas et al. 2005, Fig. 3).

Fig 5.13 shows that a large portion of the total H_2 S(3) emission (approximately 45%) comes from within a region around the southern nucleus. The strongest H_2 emitter in the active overlap region is 'longwave'. We overlaid the contours of the ISO H_2 S(3) intensity map (Haas et al. 2005). 'longwave' is close to the southern peak of the contour map. However, the northern peak of the contour map has no luminous counterpart in our map. Our closest peak is 'fuzz', which contains more than an order of magnitude less H_2 mass than 'longwave'. This is independently confirmed by the pointed 'hires' spectrum, which includes the S(1) line to account for colder H_2 gas as well.

5.4.10 H_2 excitation mechanisms

As discussed in Section 5.3.4, H_2 emission can be excited in different ways. Unfortunately, the mid-infrared pure rotational lines are not a good discriminant since the lines' critical densities are low. The near-infrared rotation-vibration transitions 2-1 S(1) at 2.248μm and 1-0 S(1) at 2.122μm can be used to discriminate between shocks and UV excitation (e.g., Takami et al. 2000). Their ratio is typically 0.1 in shocked regions (with the gas in LTE at $T \sim 2 \cdot 10^3$ K), but ~ 0.6 for "pure" UV fluorescence (Black & van Dishoeck 1987). However, in very dense PDRs ($\sim 10^5$ cm^{-3}) even the near-infrared rotation-vibrational lines are not a good discriminant anymore as thermal collisions can transfer the lower-level ($\nu < 2$) populations toward that in LTE, and line ratios will resemble those observed in shocked regions (e.g., Sternberg & Dalgarno 1989). In Chapter 4 we derived H_2 2-1 S(1) / H_2 1-0 S(1) values between 0.15 and 0.34 for peaks 1, 2, and longwave. These values are in the "grey zone" between the model values for UV pumping and shocks. However, since thermal collisions may lower the ratios, we assume that the H_2 gas is predominantly excited (directly or indirectly) from the H II regions. The presence of high ν-level lines ($\nu = 4, 5, 6, 7$) further demonstrates that fluorescence plays an important role (Chapter 4). From various diagnostics Schulz et al. (2007) also concluded that, at present, massive shock heating, either due to supernova remnants or due to cloud collisions, is not likely the dominant heating source for the GMCs in the overlap region.

The only exception may be the nucleus of NGC 4039 for which – to our knowledge – no published near-infrared H_2 flux measurements exist, but the spectra of Gilbert et al. (2000) and Mengel et al. (2001) suggest that the H_2 2-1 S(1) / 1-0 S(1) ratio is very small and lies within the 'shocked' regime. Based on the near-infrared lines of H_2 1-0 S(1) and Brγ, Fischer et al. (1996) argued that the H_2 surface brightness at the nucleus of NGC 4039 is too high to be explained by UV excitation, and favoured C-shocks.

Haas et al. (2005) found exceptionally strong H_2 S(3) emission from the overlap region in ISO data, which is also spatially displaced from the known starburst regions (Fig. 5.13). They interpret these two findings as combined evidence for pre-starburst shocks that arise from neutral H I cloud-cloud collisions. These cloud-cloud collisions would constitute a pressure wave, which in turn shocks the H_2 clouds. The IRS spectral maps do not confirm the ISOCAM S(3) detections reported by Haas et al. (2005), neither their spatial distribution nor their line luminosity. Our independent observations with the IRS-SH spectrograph agree reasonably well (Table 5.7) with the flux distribution in the spectral maps. We have also checked the IRS-LL map, which includes the H_2S(1) emission line, albeit at two times lower spatial resolution, and confirmed the strong drop in H_2 emission north-ward of peak 3. Altogether, we cannot confirm the claim of strong H_2 emission from a region extending farther to the north of the overlap region, well beyond the most active area.

Apart from the nucleus of NGC 4039, the H_2 emission appears to be well correlated with the starburst activity in the southern part of the overlap region and traces the SSCs quite well. We conclude that this argues against pre-starburst shocks due to H I cloud-cloud collisions resulting from the galaxies interaction. Based on the low cluster-to-cluster velocity dispersion of < 10 km s^{-1} Whitmore et al. (2005) also concluded that

high velocity cloud-cloud collisions are not playing a major role. However, we cannot unambiguously distinguish between local shocks and UV excitation. The near-infrared line diagnostics favour UV excitation in dense PDRs, but the small spatial offset observed in a few positions between the S(2) line and the continuum (Section 5.4.4) may argue for local shocks, e.g. from supernovae. Further observations at higher resolution, e.g. by JWST, are necessary to resolve this puzzle.

5.5 Summary

We observed the Antennae galaxies (NGC 4038/39) with the Infrared Spectrograph onboard of the Spitzer Space Telescope to study the properties of the ISM and the most luminous super star clusters in this prototype merger system. We obtained low-resolution ($R \sim 100$) spectral maps of the entire central area and high-resolution ($R \sim 600$) spectra of six super star clusters and the two galactic nuclei. The high signal-to-noise spectra allow for a detailed study of fine-structure lines, PAHs, silicates and molecular hydrogen in the range between $5 - 38\mu$m.

We found that the nucleus of NGC 4038 is relatively inactive while NGC 4039 has associated starburst activity. For both nuclei we do not find evidence for an actively accreting nucleus. By far the strongest radiation field originates from two compact clusters in the overlap region. The PDRs are generally more extended and can be found throughout the overlap region. The H_2 emission is quite strong but rather confined to the nucleus of NGC 4039 and the southern, more active, part of the overlap region.

We investigated the six SSCs in detail and found that their mid-infrared continuum slope, representative of the dust temperature, is very similar to that of starburst galaxies. The star formation rate of these clusters together, which represents a significant fraction of the total SFR in the Antennae, is approximately $6 M_\odot/\mathrm{yr}$.

The strength of the PAH emission depends critically on the radiation field. Regions with stronger radiation fields show reduced PAH emission. However, we have shown that the results are dependent on the spatial resolution of the instrument. We found no evidence for PAH ionization effects or grain size variations from the PAH spectrum, nor did we find a correlation between the H_2 line fluxes and PAH fluxes. In fact, we find an obvious lack of correspondence between the H_2 and the PAH maps, although both species are thought to originate from the same regions. However, we noticed that the PAH fluxes scale with the temperature of the H_2 gas – warmer PDRs are more efficient PAH emitters. Furthermore, the temperature of the H_2 gas anti-correlates with the [Ne III]/[Ne II] ratio, which is possibly due to the evolution of the geometry of the ISM surrounding the clusters.

The average H_2 temperature in the star forming regions is 295 K. We calculated a total mass of warm H_2 in the Antennae of $2.5 \cdot 10^7 M_\odot$, which leads to a fraction of warm to total H_2 mass of less than 0.5%. We cannot confirm the exceptionally strong H_2 S(3) emission that was previously reported based on ISOCAM-CVF data, but near-infrared H_2 lines reveal the importance of UV-excitation (Chapter 4). Whether the H_2 emission is primarily due to local shocks or UV pumping cannot be unambiguously determined from our data. However, based on line strengths and the spatial flux distribution we can rule out pre-starburst shocks resulting from the interaction as the dominating ex-

citation mechanism.

Acknowledgments

We would like to thank Martin Haas for many critical remarks on the H_2 emission. Special thanks go to Dr. Zhong Wang, who provided the proprietary IRAC images of the Antennae to us right after the observations, which enabled the optimal planning of our spectroscopic follow-up.
This work is based on observations made with the *Spitzer* Space Telescope, which is operated by the Jet Propulsion Laboratory, California Institute of Technology under NASA contract 1407. Support for this work was provided by NASA through Contract Number 1257184 issued by JPL/Caltech.

References

Anders, P., Bissantz, N., Boysen, L., de Grijs, R., & Fritze-v. Alvensleben, U. 2007, MNRAS 377, 91
Bakes, E.L.O. & Tielens, A.G.G.M., 1994, ApJ 427, 822
Baldi, A., Raymond, J. C., Fabbiano, G., Zezas, A., Rots, A. H., Schweizer, F., King, A. R., & Ponman, T. J. 2006, ApJS 162, 113
Baldi, A., Raymond, J. C., Fabbiano, G., Zezas, A., Rots, A. H., Schweizer, F., King, A. R., & Ponman, T. J. 2006, ApJ 636, 158
Bastian, N., Emsellem, E., Kissler-Patig, M. & Maraston, C., 2006, A&A 445, 471
Bastian, N., Saglia, R.P., Goudfrooij, P., Kissler-Patig, M., Maraston, C., Schweizer, F., & Zoccali, M. 2006, A&A 448, 881
Beck, S. C., Lacy, J. H., & Geballe, T. R. 1979, ApJL 234, L213
Beirão, P., Brandl, B., Devost, D., Smith, J.D., Hao, L., Houck, J.R., 2006, ApJL 643, L1
Black, J.H. & van Dishoeck, E.F., 1987, ApJ 322, 412
Brandl, B. R. et al, 2005, ApJ 635, 280
Brandl, B.R., et al. 2006, ApJ 653, 1129
Burton, M.G., Hollenbach, D.J., Tielens, A.G. 1992, ApJ 399, 563
Cesarsky, D., Lequeux, J., Abergel, A., Perault, M., Palazzi, E., Madden, S., Tran, D., 1996, A&A 315, 309
Chiar, J.E., Ennico, K., Pendleton, Y.J., Greene, T., Knez, C., Lada, C., Roellig, T., Tielens, A.G.G.M., Werner, M., & Whittet, D.C.B., 2007 (arXiv:0707.3480)
Clark, D. M., et al. 2007, ApJ 658, 319
de La Fuente Marcos, R., & de La Fuente Marcos, C. 2006, MNRAS 372, 279
Devost, D., et al. 2007, ApJ submitted
Draine, B. T., Roberge, W. G. & Dalgarno, A., 1983, ApJ 264, 48
Draine, B.T., 1989, Proceedings of the 22nd Eslab Symposium, ed. B.H. Kaldeich, ESA SP-290, 93
Draine, B. T. & Woods, D. T., 1992, ApJ 387, 732
Draine, B. T. & Li, A., 2001, ApJ 551, 807
Draine, B. T. & Li, A., 2007, ApJ 657, 810
Fall, S. M., Chandar, R., & Whitmore, B. C. 2005, ApJL 631, L133
Feng, H., & Kaaret, P. 2006, ApJ 653, 536
Fischer et al. 1996, A&A 315, L97
Förster Schreiber, Sauvage, M.,Charmandaris, V., Laurent, O., Gallais, P., Mirabel, I.F., Vigroux, L., 2003, A&A 399, 833
Fritze-v. Alvensleben, U. 1999, A&A 342, L25
Gao, Y., Lo, K. Y., Lee, S.-W., & Lee, T.-H. 2001, ApJ 548, 172
Geballe, T.R., Tielens, A.G.G.M., Allamandola, L.J., Moorhouse, A., Brand, P.W.J.L., 1989, ApJ 341, 278
Gilbert, A. M. et al, 2000, ApJ 533, L57
Gilbert, A. M. & Graham, J.R., 2007, ApJ in press

Groves et al., 2007, in prep.
Haas, M., Chini, R., & Klaas, U. 2005, A&A 433, L17
Habart, E., Walmsley, M., Verstraete, L., Cazaux, S., Maiolino, R., Cox, P., Boulanger, F., & Des Forêts, G. P. 2005, Space Science Reviews, 119, 71
Higdon, S.J.U., Devost, D., Higdon, J.L., Brandl, B.R., Houck, J.R., Hall, P., Barry, D., Charmandaris, V., Smith, J.D.T., Sloan, G.C., Green, J., 2004, PASP 116, 975
Higdon, S.J.U., Armus, L., Higdon, J.L., Soifer, B.T., & Spoon, H.W.W., 2006, ApJ 648, 323
Hollenbach, D.J. & Tielens, A.G.G.M., 1997, ARA&A 35, 179
Houck, J. R. et al., 2004, ApJS 154, 18
Hudgins, D.M. & Allamandola, L.J. 1995, J. Phys. Chem., 99, 3033
Joblin, C., Tielens, A.G.G.M., Geballe, T.R., Wooden, T.H. 1996, ApJL 460, L119
Kassin, S.A., Frogel, J.A., Pogge, R.W., Tiede, G.P., & Sellgren, K. 2003, AJ 126, 1276
Kennicutt, R.C., 1998, ARA&A 36, 189
Klaas, U., Haas, M., Heinrichsen, I., Schulz, B., 1997, A&A 325, L21
Kunze et al. 1996, A&A 315, L101
Larson, R.B. & Tinsley, B.M. 1978, ApJ 219, 46
Lepp, S. & McCray, R. 1983, ApJ 269, 560
Leitherer, C., et al. 1999, ApJS, 123, 3
Lutz, D., Kunze, D., Spoon, H.W.W., Thornley, M.D., 1998, A&A 333, 75
Lutz, D., 1999, in *The Universe as seen by ISO*, Paris, 20 − 23 Oct. 1998, ESA SP-427, 623
Martín-Hernández, N.L., Schaerer, D., Peeters, E., Tielens, A.G.G.M., Sauvage, M. 2006, A&A 455, 853
Mathis, J. S. 1990, ARA&A 28, 37
Mengel, S., Lehnert, M. D., Thatte, N., Tacconi-Garman, L. E. & Genzel, R., 2001, ApJ 550, 280
Mengel, S., Lehnert, M. D., Thatte, N. & Genzel, R., 2002, A&A 383, 137
Mengel, S., Lehnert, M. D., Thatte, N. & Genzel, R., 2005, A&A 443, 41
Mihos, J. C., & Hernquist, L. 1996, ApJ 464, 641
Mirabel, I. F. et al. 1998, A&A 333, L1
Moneti, A., Stolovy, S., Blommaert, J.A., Figer, D.F., & Najarro, F. 2001, A&A 366, 106
Moorwood, A. F. M. & Oliva, E., 1994, ApJ 429, 602
Murtagh, F., Starck, J.-L., Bijaoui, A. 1995, A&AS 112, 179
Neff, S. G., et al. 1996, BAAS 28, 826
Neff, S. G. & Ulvestad, J. S., 2000, AJ 120, 670
Nikola, T., Genzel, R., Herrmann, F., Madden, S.C., Poglitsch, A., Geis, N., Townes, C.H., & Stacey, G.J., 1998, ApJ 504, 749
Östlin, G., Cumming, R.J., & Bergvall, N. 2007, A&A 461, 471
Rigopoulou, D., Spoon, H.W.W., Genzel, R., Lutz, D., Moorwood, A.F.M., Tran, Q.D., 1999, AJ 118, 2625
Rigopoulou, D., Kunze, D., Lutz, D., Genzel, R., & Moorwood, A. F. M. 2002, A&A 389, 374
Roche, P.F. & Aitken, D.K., 1984, MNRAS 208, 481
Rosenthal, D., Bertoldi, F., Drapatz, S. 2000 A&A 356, 705
Roussel, H., Helou, G., Hollenbach, D.F., Draine, B.T., Smith, J.D., Armus, L., Schinnerer, E., Walter, F., Engelbracht, C.W., Thornley, M.D., Kennicutt, R.C., Calzetti, D., Dale, D.A., Murphy, E.J., Bot, C., 2007 (arXiv:0707.0395)
Salpeter, E.E., 1955, ApJ 123, 666
Sanders, D. B. & Mirabel, I.F., ARA&A 34, 749
Saviane, I., Hibbard, J. E., Rich, M. R. 2004, AJ 127, 660
Schulz, A., Henkel, C., Muders, D., Mao, R. Q., Röllig, M., & Mauersberger, R. 2007, A&A 466, 467
Shull, J.M. & Hollenbach, D.J., 1978, ApJ 220, 525
Smith, J.D. et al.(2006) http://turtle.as.arizona.edu/jdsmith/cubism.php
Smith J. D. et al, 2007, ApJ 656, 770
Snijders, L., van der Werf, P. P., Brandl, B. R., Mengel, S., Schaerer, D., & Wang, Z. 2006, ApJL 648, L25
Snijders, L., Kewley, L. J. & van der Werf, P. P., 2007, ApJ accepted
Soifer, B.T., Boehmer, L., Neugebauer, G., & Sanders, D.B., 1989, AJ 98, 766
Spitzer Observer's Manual, 2004, `http://ssc.spitzer.caltech.edu/documents/SOM/`
Spoon, H. W. W., Marshall, J. A., Houck, J. R., Elitzur, M., Hao, L., Armus, L., Brandl, B. R., & Charman-

daris, V. 2007, ApJL 654, L49
Stanford, S. A., Sargent, A. I., Sanders, D. B. & Scoville, N. Z., 1990, ApJ 349, 492
Sternberg, A. & Dalgarno, A., 1989, ApJ 338, 197
Sternberg, A., & Neufeld, D. A. 1999, ApJ 516, 371
Strickland, D. K., & Stevens, I. R. 2000, MNRAS 314, 511
Sturm, E., Lutz, D., Tran, D., Feuchtgruber, H., Genzel, R., Kunze, D., Moorwood, A.F.M., Thornley, M.D., 2000, A&A 358, 481
Takahashi, J, 2001, ApJ 561, 254
Takami, M., Usuda, T., Sugai, H., Kawabata, H., Suto, H., & Tanaka, M. 2000, ApJ 529, 268
Tielens, A. G. G. M. & Hollenbach, 1985, ApJ 291, 722
Tielens, A. G. G. M., 2005, "The Physics and Chemistry of the Interstellar Medium", Cambridge University Press
Toomre, A. 1977, in *The Evolution of Galaxies and Stellar Populations*, ed. B. M. Tinsley, & R. B. Larson (New Haven: Yale Univ. Press), 401
Tran, Q.D., 1998, Ph.D. Thesis, Université de Paris XI
Turner, J. L. & Beck, S. C., 2004, ApJ 602, 85
Valentijn, E. A., van der Werf, P. P., de Graauw, T., & de Jong, T. 1996, A&A 315, L145
van Kerckhoven, C., et al. 2000, A&A 357, 1013
Vermeij, R., Peeters, E., Tielens, A.G.G.M., van der Hust, J.M., 2002, A&A 382, 1042
Verstraete, L., Puget, J.L., Falgarone, E., Drapatz, S., Wright, C.M., Timmermann, R., 1996, A&A 315, 337
Vigroux, L. et al. 1996, A&A 315, L93
Wang, Z., et al. 2004, ApJS 154, 193
Weedman, D. W., Feldman, F. R., Balzano, V. A., Ramsey, L. W., Sramek, R. A. & Wu, C.-C., 1981, ApJ 248, 105
Weedman, D.W., Hao, L., Higdon, S.J.U., Devost. D., Wu, Y., Charmandaris, V., Brandl, B.R., Armus, L., Spoon, H.W.W., Bass, E., Houck, J.R., 2005, ApJ 633, 706
Van der Werf, P. P., Genzel, R., Krabbe, A., Blietz, M., Lutz, D., Drapatz, S., Ward, M. J. & Forbes, D. A., 1993, ApJ 405, 522
Werner, M. et al., 2004, ApJS 154, 1
Wilson, C. D., Scoville, N., Madden, S. C.& Charmandaris, V., 2000, ApJ 542, 120
Whitmore, B. W. & Schweizer, F., 1995, AJ 109, 960
Whitmore, Bradley C. et al., 1999, AJ 118, 1551
Whitmore, B. W. & Zhang, Q., 2002, AJ 124, 1418
Whitmore, B. W. et al, 2005, AJ 130,2104
Whitmore, B. C., Chandar, R., & Fall, S. M. 2007, AJ, 133, 1067
Wu, Y., Charmandaris, V., Hao, L., Brandl, B.R., Bernard-Salas, J., Spoon, H.W.W., Houck, J.R., 2005, ApJ 639, 157
Zezas, A., Fabbiano, G., Rots, A. H., & Murray, S. S. 2002, ApJ 577, 710
Zezas, A., Fabbiano, G., Rots, A.H.& Murray, S.S. 2002, ApJS 142, 239
Zezas, A., Fabbiano, G., Baldi, A., Schweizer, F., King, A. R., Ponman, T. J., & Rots, A. H. 2006, ApJS 166, 211
Zezas, A., Fabbiano, G., Baldi, A., Schweizer, F., King, A. R., Rots, A. H., & Ponman, T. J. 2007, ApJ 661, 135
Zhang, Q., Fall, M. F., & Whitmore, B. C., 2001, ApJ 561, 727